Electronic and thermoelectric properties of van der Waals materials with ring-shaped valence bands

Darshana Wickramaratne,[1,a)] Ferdows Zahid,[2] and Roger K. Lake[1,a)]
[1]*Laboratory for Terahertz and Terascale Electronics, Department of Electrical and Computer Engineering, University of California, Riverside, California 92521, USA*
[2]*Department of Physics and the Center of Theoretical and Computational Physics, The University of Hong Kong, Pokfulam Road, Hong Kong, China*

(Received 13 June 2015; accepted 1 August 2015; published online 17 August 2015)

The valence band of a variety of few-layer, two-dimensional materials consist of a ring of states in the Brillouin zone. The energy-momentum relation has the form of a "Mexican hat" or a Rashba dispersion. The two-dimensional density of states is singular at or near the band edge, and the band-edge density of modes turns on nearly abruptly as a step function. The large band-edge density of modes enhances the Seebeck coefficient, the power factor, and the thermoelectric figure of merit ZT. Electronic and thermoelectric properties are determined from *ab initio* calculations for few-layer III–VI materials GaS, GaSe, InS, InSe, for Bi_2Se_3, for monolayer Bi, and for bilayer graphene as a function of vertical field. The effect of interlayer coupling on these properties in few-layer III–VI materials and Bi_2Se_3 is described. Analytical models provide insight into the layer dependent trends that are relatively consistent for all of these few-layer materials. Vertically biased bilayer graphene could serve as an experimental test-bed for measuring these effects. © *2015 AIP Publishing LLC*. [http://dx.doi.org/10.1063/1.4928559]

I. INTRODUCTION

The electronic bandstructure of many two-dimensional (2D), van der Waals (vdW) materials qualitatively change as the thickness is reduced down to a few monolayers. One well known example is the indirect to direct gap transition that occurs at monolayer thicknesses of the Mo and W transition metal dichalcogenides (TMDCs).[1] Another qualitative change that occurs in a number of 2D materials is the inversion of the parabolic dispersion at a band extremum into a "Mexican hat" dispersion.[2–4] Mexican hat dispersions are also referred to as a Lifshitz transition,[3,5,6] an electronic topological transition,[7] or a camel-back dispersion.[8,9] In a Mexican hat dispersion, the Fermi surface near the band-edge is approximately a ring in k-space, and the radius of the ring can be large, on the order of half of the Brillouin zone. The large degeneracy coincides with a singularity in the two-dimensional (2D) density of states close to the band edge. A similar feature occurs in monolayer Bi due to the Rashba splitting of the valence band.[10] This also results in a valence band edge that is a ring in k-space although the diameter of the ring is generally smaller than that of the Mexican hat dispersion.

Mexican hat dispersions are relatively common in few-layer two-dimensional materials. *Ab-initio* studies have found Mexican hat dispersions in the valence band of many few-layer III–VI materials such as GaSe, GaS, InSe, and InS.[3,4,11–14] Experimental studies have demonstrated synthesis of monolayers and or few layers of GaS, GaSe, and InSe thin films.[11,15–20] Monolayers of Bi_2Te_3[21] and Bi_2Se_3[22] also exhibit a Mexican hat dispersion in the valence band. The conduction and valence bands of bilayer graphene distort into Mexican hat dispersions when a vertical field is applied across AB-stacked bilayer graphene.[2,6,23] The large density of states of the Mexican hat dispersion can lead to instabilities near the Fermi level, and two different *ab initio* studies have recently predicted Fermi-level controlled magnetism in monolayers GaSe and GaS.[13,14] The singularity in the density of states and the large number of conducting modes at the band edge can enhance the Seebeck coefficient, power factor, and the thermoelectric figure of merit ZT.[24–26]

The thermoelectric figure of merit of a material is the dimensionless quantity ZT. The traditional approaches to maximize ZT are to reduce the lattice thermal conductivity[27–29] or increase the power factor (PF)[30,31] by enhancing the electronic density of states. Prior studies have achieved this enhancement in the density of states by using nanowires,[32,33] nanoparticles,[31] doping levels,[25,26,30] high band degeneracy,[34–36] and using the Kondo resonance associated with the presence of localized d and f orbitals.[37–39] The non-parabolic band distortions that occur in low-dimensional, 2D materials also give rise to enhanced density of states near band edges. An early analytical study found a factor of 5 enhancement in the thermopower resulting from a Lifshitz transition.[40] Analytical studies found that the thermopower in a two-dimensional electron gas and in monolayer graphene can be enhanced due to the presence of Rashba interaction.[41,42] *Ab-initio* calculations have been used to connect the complex Fermi-surfaces of bulk materials with their favorable thermoelectric properties. For example, in bulk Na_xCoO_2 and electron-doped $FeAs_2$, the "pudding-mold" shaped Fermi surface of the valence band and conduction band, respectively, of each material leads to large enhancements in the thermopower.[43–46] The enhanced thermopower in PbTe, PbSe, PbS, and SnTe was explained by their complex "pipe" shaped Fermi-surfaces.[47] Bulk Bi_2Se_3, Bi_2Te_3,

a)Authors to whom correspondence should be addressed. Electronic addresses: darshanaw@engineering.ucsb.edu and rlake@ece.ucr.edu

and Bi_2Te_2Se exhibit non-parabolic features in their valence band due to the band-inversion associated with their topological insulating properties.[48,49] The non-parabolic features in the valence band of these materials explained the favorable thermoelectric properties exhibited by this class of materials. The large increase in ZT predicted for monolayer Bi_2Te_3 resulted from the formation of a Mexican hat bandstructure and its large band-edge degeneracy.[21,50,51]

Motivated by the aforementioned studies, this work theoretically investigates the electronic and thermoelectric properties of a variety of van der Waals materials that exhibit a Mexican hat dispersion or Rashba dispersion. The Mexican hat and Rashba dispersions are first analyzed using an analytical model. Then, density functional theory is used to calculate the electronic and thermoelectric properties of bulk and one to four monolayers of GaX, InX (X = Se, S), Bi_2Se_3, monolayer Bi(111), and bilayer graphene as a function of vertical electric field. Figure 1 illustrates the investigated structures that have either a Mexican hat or Rashba dispersion. The analytical model combined with the numerically calculated orbital compositions of the conduction and valence bands explain the layer dependent trends that are relatively consistent for all of the few-layer materials. While numerical values are estimated for various thermoelectric metrics, the goal of this work is to understand the layer-dependent bandstructure trends and their effect on the electronic and thermoelectric properties. The metrics are provided in such a way that new estimates can be readily obtained given new values for the electrical or thermal conductivity.

II. MODELS AND METHODS

A. Landauer thermoelectric parameters

In the linear response regime, the electronic and thermoelectric parameters are calculated within a Landauer formalism. The basic equations and their equivalence to standard equations resulting from the Boltzmann transport equation have been described previously,[52,53] and we list them below for convenience. The equations for the electronic conductivity (σ), the electronic thermal conductivity (κ_e), and the Seebeck coefficient (S) are

$$\sigma = (2q^2/h)I_0 \quad (\Omega^{-1}\mathrm{m}^{2-\mathrm{D}}), \tag{1}$$

$$\kappa_e = (2Tk_B^2/h)(I_2 - I_1^2/I_0) \quad (\mathrm{Wm}^{2-\mathrm{D}}\mathrm{K}^{-1}), \tag{2}$$

$$S = -(k_B/q)\frac{I_1}{I_0} \quad (\mathrm{V/K}), \tag{3}$$

with

$$I_j = L\int_{-\infty}^{\infty}\left(\frac{E-E_F}{k_BT}\right)^j \bar{T}(E)\left(-\frac{\partial f}{\partial E}\right)dE, \tag{4}$$

where L is the device length, D is the dimensionality (1, 2, or 3), q is the magnitude of the electron charge, h is Planck's constant, k_B is Boltzmann's constant, and f is the Fermi-Dirac factor. In the diffusive limit, the transmission function $\bar{T}$ is

$$\bar{T}(E) = M(E)\lambda(E)/L, \tag{5}$$

where M(E) as the density of modes, and $\lambda(E)$ is the electron mean free path. The power factor (PF) and the thermoelectric figure of merit (ZT) are given by $PF = S^2\sigma$ and

$$ZT = S^2\sigma T/(\kappa_l + \kappa_e), \tag{6}$$

where κ_l is the lattice thermal conductivity.

B. Analytical models

As the thicknesses of the layered materials are reduced to a few monolayers, the valence band dispersion transitions from parabolic to Mexican hat. In this section, we consider analytical models to understand the effect of this band inversion on the electronic and thermoelectric properties. The trends and insight provided by the analytical models provide a guide to understanding the numerical results that follow.

The single-spin density of modes for transport in the x direction is[52,54]

$$M(E) = \frac{2\pi}{L^D}\sum_{\mathbf{k}}\delta(E-\epsilon(\mathbf{k}))\frac{\partial\epsilon}{\partial k_x}, \tag{7}$$

where D is the dimensionality, E is the energy, and $\epsilon(\mathbf{k})$ is the band dispersion. The sum is over all values of $\mathbf{k}$ such that $\frac{\partial\epsilon}{\partial k_x} > 0$, i.e., all momenta with positive velocities. The dimensions are $1/L^{D-1}$, so that in 2D, $M(E)$ gives the number of modes per unit width at energy E. If the dispersion is only a function of the magnitude of $\mathbf{k}$, then Eq. (7) reduces to

$$M(E) = \frac{N_D}{(2\pi)^{D-1}}\sum_b k_b^{D-1}(E), \tag{8}$$

where $N_D = \pi$ for $D = 3$, $N_D = 2$ for $D = 2$, and $N_D = 1$ for $D = 1$. k_b is the magnitude of $\mathbf{k}$ such that $E = \epsilon(k_b)$, and the sum is over all bands and all values of k_b within a band. When a band-edge is a ring in k-space with radius k_0, the single-spin 2D density of modes at the band edge is

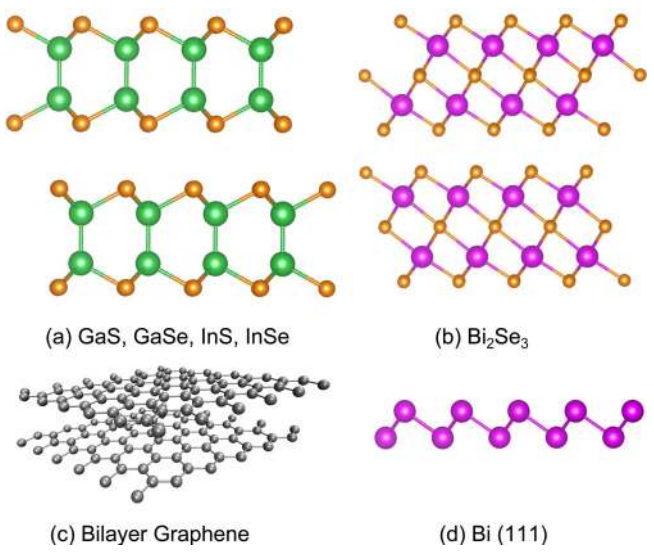

FIG. 1. Atomic structures of van-der Waals materials with a Mexican hat or Rashba dispersion: (a) Bilayer III-VI material. The β phase stacking geometry is illustrated. (b)Bi_2Se_3, (c) bilayer graphene, and (d) Bi(111) monolayer.

$$M(E_{\text{edge}}) = N\frac{k_0}{\pi}, \tag{9}$$

where N is either 1 or 2 depending on the type of dispersion, Rashba or Mexican hat. Thus, the 2D density of modes at the band edge depends only on the radius of the k-space ring. For a two dimensional parabolic dispersion, $E = \frac{\hbar^2 k^2}{2m^*}$, the radius is 0, and Eq. (8) gives a the single-spin density of modes of[55]

$$M_{\text{par}}(E) = \frac{\sqrt{2m^* E}}{\pi\hbar}. \tag{10}$$

In real III–VI materials, there is anisotropy in the Fermi surfaces, and a 6th order, angular dependent polynomial expression is provided by Zólyomi *et al*. that captures the low-energy anisotropy.[3,4] To obtain physical insight with closed form expressions, we consider a 4th order analytical form for an isotropic Mexican hat dispersion

$$\epsilon(k) = \epsilon_0 - \frac{\hbar^2 k^2}{2m^*} + \frac{1}{4\epsilon_0}\left(\frac{\hbar^2 k^2}{2m^*}\right)^2, \tag{11}$$

where ϵ_0 is the height of the hat at $k = 0$, and m^* is the magnitude of the effective mass at $k = 0$. A similar quartic form was previously used to analyze the effect of electron-electron interactions in biased bilayer graphene.[2] The function is plotted in Figure 2(a). The band edge occurs at $\epsilon = 0$, and, in k-space, in two dimensions (2D), it forms a ring in the $k_x - k_y$ plane with a radius of

$$k_0^{\text{MH}} = \frac{2\sqrt{m^*\epsilon_0}}{\hbar}. \tag{12}$$

For the two-dimensional Mexican hat dispersion of Eq. (11), the single-spin density of modes is

$$M_{\text{MH}}(E) = \begin{cases} \frac{k_0^{\text{MH}}}{\pi}\left(\sqrt{1+\sqrt{\frac{E}{\epsilon_0}}} + \sqrt{1-\sqrt{\frac{E}{\epsilon_0}}}\right) & (0 \le E \le \epsilon_0) \\ \frac{k_0^{\text{MH}}}{\pi}\left(\sqrt{1+\sqrt{\frac{E}{\epsilon_0}}}\right) & (\epsilon_0 \le E). \end{cases} \tag{13}$$

Figure 2(b) shows the density of mode distributions plotted from Eqs. (10) and (13). At the band edge ($E = 0$), the single-spin density of modes of the Mexican hat dispersion is finite

$$M_{\text{MH}}(E = 0) = \frac{2k_0^{\text{MH}}}{\pi}. \tag{14}$$

The Mexican hat density of modes decreases by a factor of $\sqrt{2}$ as the energy increases from 0 to ϵ_0, and then it slowly increases. The step-function turn-on of the density of modes is associated with a singularity in the density of states. The single-spin density of states resulting from the Mexican hat dispersion is

$$D_{\text{MH}}(E) = \begin{cases} \frac{m^*}{\pi\hbar^2}\sqrt{\frac{\epsilon_0}{E}} & (0 \le E \le \epsilon_0) \\ \frac{m^*}{2\pi\hbar^2}\sqrt{\frac{\epsilon_0}{E}} & (\epsilon_0 < E). \end{cases} \tag{15}$$

Rashba splitting of the spins also results in a valence band edge that is a ring in k-space. The Bychkov-Rashba model with linear and quadratic terms in k gives an analytical expression for a Rashba-split dispersion[56]

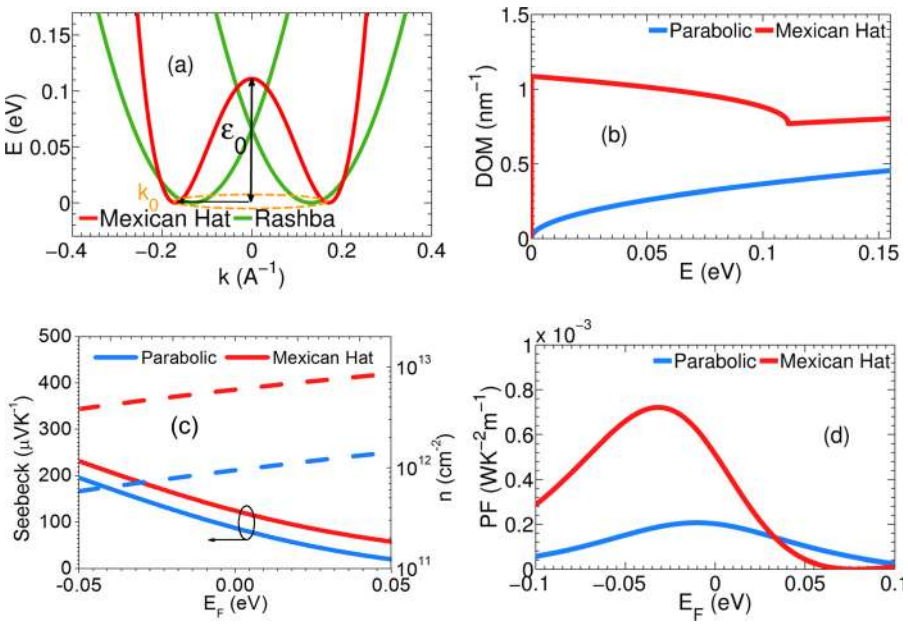

FIG. 2. (a) Comparison of a Mexican hat dispersion (red) and a Rashba dispersion (green). The band edges are rings in k-space with radius k_0 illustrated for the Mexican hat band by the orange dotted circle. The height of the Mexican hat band at $k = 0$ is $\epsilon_0 = 0.111$ eV. The Rashba parameter is 1.0 eV Å, and the effective mass for both dispersions is $0.5m_0$. (b) Density of modes of the Mexican hat dispersion (red) versus parabolic band (blue). The parabolic dispersion also has an effective mass of $0.5m_0$. (c) Room temperature Seebeck coefficients (solid lines) and carrier concentrations (broken lines) of the Mexican hat band (red) and the parabolic band (blue) as a function of Fermi level position, E_F. (d) Room temperature ballistic power factor of the Mexican hat band (red) and the parabolic band (blue) calculated from Eqs. (1), (3), and (4) with $T(E) = 1$.

$$\epsilon(\mathbf{k}) = \epsilon_0 + \frac{h^2k^2}{2m^*} \pm \alpha_R k, \tag{16}$$

where the Rashba parameter, α_R, is the strength of the Rashba splitting. In Eq. (16), the bands are shifted up by $\epsilon_0 = \frac{\alpha_R^2 m^*}{2\hbar^2}$ so that the band edge occurs at $\epsilon = 0$. The radius of the band edge in k-space is

$$k_0^{\mathrm{R}} = \frac{m^*\alpha_R}{\hbar^2} = \frac{\sqrt{2m^*\epsilon_0}}{\hbar}. \tag{17}$$

The energy dispersion of the split bands is illustrated in Figure 2(a). The density of modes, *including both spins*, resulting from the dispersion of Eq. (16) is

$$M_{\mathrm{R}}^{2\,\mathrm{spins}}(E) = \begin{cases} \frac{2k_0^{\mathrm{R}}}{\pi} & (0 \le E \le \epsilon_0) \\ \frac{2k_0^{\mathrm{R}}}{\pi}\sqrt{\frac{E}{\epsilon_0}} & (\epsilon_0 \le E). \end{cases} \tag{18}$$

For $0 \le E \le \epsilon_0$, the density of modes is a step function and the height is determined by α_R and the effective mass. Values for α_R vary from 0.07 eV Å in InGaAs/InAlAs quantum wells to 0.5 eV Å in the Bi(111) monolayer.[57] The density of states including both spins is

$$D_{\mathrm{R}}(E) = \begin{cases} \frac{m^*}{\pi\hbar^2}\sqrt{\frac{\epsilon_0}{E}} & (0 \le E \le \epsilon_0) \\ \frac{m^*}{\pi\hbar^2} & (\epsilon_0 < E). \end{cases} \tag{19}$$

In general, we find that the diameter of the Rashba k-space rings are less than the diameter of the Mexican hat k-space rings, so that the enhancements to the thermoelectric parameters are less from Rashba-split bands than from the inverted Mexican hat bands.

Figure 2(c) compares the Seebeck coefficients and the electron densities calculated from the Mexican hat dispersion shown in Fig. 2(a) and a parabolic dispersion. The quantities are plotted versus Fermi energy with the conduction band edge at $E = 0$. An electron effective mass of $m^* = 0.5m_0$ is used for both dispersions, and, for the Mexican hat, $\epsilon_0 = 0.111$ eV which is the largest value for ϵ_0 obtained from our *ab-initio* simulations of the III–VI compounds. The temperature is $T = 300$ K. The Seebeck coefficients are calculated from Eqs. (3)–(5) with $T(E) = 1$. The electron densities are calculated from the density of state functions given by two times Eq. (15) for the Mexican hat dispersion and by $m^*/\pi\hbar^2$ for the parabolic dispersion. The electron density of the Mexican hat dispersion is approximately 6 times larger than that of the parabolic dispersion at a fixed Fermi energy. This is a result of the singular density of states at the bandedge of the Mexican hat dispersion. There are two important points to take away from this plot. At the same electron density, the Fermi level of the Mexican hat dispersion is much lower than that of the parabolic dispersion. As a result, at the same electron density, the Seebeck coefficient of the Mexican hat dispersion is much larger than the Seebeck coefficient of the parabolic dispersion.

Figure 2(d) compares the ballistic power factors calculated from the Mexican hat dispersion shown in Fig. 2(a) and the parabolic dispersion, again with $m^* = 0.5m_0$ for both dispersions. The temperature is $T = 300$ K. The ballistic power factor is calculated from Eqs. (1) and (3)–(5) with $T(E) = 1$. Eqs. (10) and (13) for the density of modes are used in Eq. (5). The peak power factor of the Mexican hat dispersion occurs when $E_F = -32$ meV, i.e., 32 meV below the conduction band edge. The peak power factor of the parabolic dispersion occurs when $E_F = -9.5$ meV. At the peak power factors, the value of I_1 of the Mexican hat dispersion is 3.5 times larger than I_1 of the parabolic dispersion, and I_0 of the Mexican hat dispersion is 3.2 times larger than I_0 of the parabolic dispersion. I_0 gives the conductivity, the ratio I_1/I_0 gives the Seebeck coefficient, and I_1^2/I_0 gives the power factor. Therefore, the inversion of the parabolic band into a Mexican hat band results in an increase in the Seebeck coefficient and a large increase in the peak power factor. This is the trend that we consistently observe in the numerical simulations as the bands invert from a parabolic to a Mexican hat dispersion as the number of layers is reduced.

From the Landauer-Büttiker perspective of Eq. (5), the increased conductivity results from the increased number of modes near the bandedge as shown in Fig. 2(b). From a more traditional perspective, the increased conductivity results from an increased density of states resulting in an increased charge density n. At their peak power factors, the charge density of the Mexican hat dispersion is 4.9×10^{12} cm^{-2}, and the charge density of the parabolic dispersion is 1.5×10^{12} cm^{-2}. The charge density of the Mexican hat dispersion is 3.3 times larger than the charge density of the parabolic dispersion even though the Fermi level for the Mexican hat dispersion is 22 meV less than the Fermi level of the parabolic dispersion. This, in general, will result in a higher conductivity. These trends are consistently followed by the numerical results. The above analytical discussion illustrates the basic concepts and trends concerning the relationship between the Mexican hat dispersion and the electronic and thermoelectric parameters, and it motivates and guides the following numerical investigation of various van der Waals materials exhibiting either Mexican hat or Rashba dispersions.

C. Computational methods

Ab-initio calculations of the bulk and few-layer structures (one to four layers) of GaS, GaSe, InS, InSe, Bi_2Se_3, Bi(111) surface, and bilayer graphene are carried out using density functional theory (DFT) with a projector augmented wave method[58] and the Perdew-Burke-Ernzerhof (PBE) type generalized gradient approximation[59,60] as implemented in the Vienna *ab-initio* Simulation Package (VASP).[61,62] The vdW interactions in GaS, GaSe, InS, InSe, and Bi_2Se_3 are accounted for using a semi-empirical Grimme-D2 correction to the Kohn-Sham energies when optimizing the bulk structures of each material.[63] All atomic positions were fully optimized until the forces acting on each atom are less than 0.01 eV/Å. The thickness of each bulk unit cell optimized with the Grimme-D2 potential is within 1.6% of the bulk experimental data for each material. For the GaX, InX

(X = S,Se), Bi(111) monolayer, and Bi_2Se_3 structures, a Monkhorst-Pack scheme is used for the integration of the Brillouin zone with a k-mesh of $12 \times 12 \times 6$ for the bulk structures and $12 \times 12 \times 1$ for the thin-films. The energy cutoff of the plane wave basis is 300 eV. The electronic band-structure calculations include spin-orbit coupling (SOC) for the GaX, InX, Bi(111), and Bi_2Se_3 compounds. To verify the results of the PBE band structure calculations of the GaX and InX compounds, the electronic structures of one to four monolayers of GaS and InSe are calculated using the Heyd-Scuseria-Ernzerhof (HSE) functional.[64] The HSE calculations incorporate 25% short-range Hartree-Fock exchange. The screening parameter μ is set to 0.2 $Å^{-1}$. For the calculations on bilayer graphene, a $32 \times 32 \times 1$ k-point grid is used for the integration over the Brillouin zone. The energy cutoff of the plane wave basis is 400 eV. 15 Å of vacuum spacing was added to the slab geometries of all few-layer structures. The optimized lattice parameters for each of the materials studied are listed in Table I below. Band structures of the monolayer and few-layer structures are calculated using the lattice constants of the optimized bulk structures. The conduction and valence band effective masses at Γ are calculated for each material by fitting the dispersion to a sixth order polynomial and then calculating $\frac{1}{m^*} = \frac{1}{\hbar^2}\frac{\partial^2 E}{\partial k^2}$.

The *ab-initio* calculations of the electronic structure are used as input for calculating the thermoelectric parameters. The two quantities required are the density of states and the density of modes. The density of states is directly provided by VASP. The density of modes calculations are performed by integrating over the first Brillouin zone using a converged k-point grid, $51 \times 51 \times 10$ k-points for the bulk structures and $51 \times 51 \times 1$ k-points for the III–VI, Bi_2Se_3 and Bi(111) thin film structures. A $101 \times 101 \times 1$ grid of k-points is required for the density of mode calculations on bilayer graphene. The details of the formalism are provided in several prior studies.[36,50,53] The temperature dependent carrier concentrations for each material and thickness are calculated from the density-of-states obtained from the *ab-initio* simulations. To obtain a converged density-of-states, a minimum k-point grid of $72 \times 72 \times 36$ ($72 \times 72 \times 1$) is required for the bulk (monolayer and few-layer) III–VI and Bi_2Se_3 structures. For the density-of-states calculations on bilayer graphene and monolayer Bi(111), a $36 \times 36 \times 1$ grid of k-points is used.

The calculation of the in-plane thermoelectric parameters, such as conductivity, the power factor, and *ZT*, requires values for the electron and hole mean free paths and the lattice thermal conductivity. Electron and hole scattering are included using an average mean free path, λ determined by matching Eq. (1) to literature conductivity data using an average value for λ in Eq. (5). The definition of the average λ is

$$\lambda = \frac{\int dE M(E)\lambda(E)\left(\frac{\partial f}{\partial E}\right)}{\int dE M(E)\left(\frac{\partial f}{\partial E}\right)}. \quad (20)$$

It is the average mean free path per mode in the thermal transport window of a few k_BT defined by $(-\partial f/\partial E)$. For all of the few-layer materials, the peak ZT occurs when E_F is in the band gap, below the conduction band edge for n-type material or above the valence band edge for p-type material. Therefore, only the low-energy states within a few k_BT of the band-edges contribute to the transport.

For GaS, GaSe, InS, and InSe, $\lambda_0 = 25$ nm gives the best agreement with experimental data.[70–73] The room temperature bulk n-type electrical conductivity of GaS, GaSe, InS, and InSe was reported to be 0.5 $\Omega^{-1}\,m^{-1}$, 0.4 $\Omega^{-1}\,m^{-1}$, 0.052 $\Omega^{-1}\,m^{-1}$, and 0.066 $\Omega^{-1}\,m^{-1}$, respectively, at a carrier concentration of $10^{16}\,cm^{-3}$. Using $\lambda_0 = 25$ nm for bulk GaS, GaSe, and InSe, we obtain an electrical conductivity of 0.58 $\Omega^{-1}\,m^{-1}$, 0.42 $\Omega^{-1}\,m^{-1}$, 0.058 $\Omega^{-1}\,m^{-1}$, and 0.071 $\Omega^{-1}\,m^{-1}$, respectively, at the same carrier concentration. For the Bi(111) monolayer surface, the electrical conductivity at 300 K is reported to be of 0.011 $\Omega^{-1}\,m^{-1}$ at a carrier concentration of $2.6 \times 10^{18}\,cm^{-3}$.[74] An electron and hole mean free path of 4.7 nm gives the best agreement with the electrical conductivity of bulk Bi. For Bi_2Se_3, an electron mean free path, $\lambda_e = 5.2$ nm, and a hole mean free path, $\lambda_p = 2.1$ nm, give the best agreement with experimental data on conductivity for bulk single crystal Bi_2Se_3.[75] The room temperature bulk n-type electrical conductivity is reported to be 1.5 $\Omega^{-1}\,m^{-1}$ at a carrier concentration of $10^{17}\,cm^{-3}$ and the p-type electrical conductivity at room temperature is 4.8 $\Omega^{-1}\,m^{-1}$ at a carrier concentration of $10^{19}\,cm^{-3}$ For bilayer graphene, $\lambda_0 = 88$ nm gives the best agreement with experimental data on conductivity at room temperature.[76]

Values for the lattice thermal conductivity are also taken from available experimental data. The experimental value of 10 $W\,m^{-1}\,K^{-1}$ reported for the in-plane lattice thermal conductivity κ_l of bulk GaS at room temperature is used for the gallium chalcogenides.[77] The experimental, bulk, in-plane, lattice thermal conductivities of 7.1 $W\,m^{-1}\,K^{-1}$ and 12.0 $W\,m^{-1}\,K^{-1}$ measured at room temperature are used for InS and InSe, respectively.[78] For monolayer Bi(111), the calculated κ_l from molecular dynamics[79] at 300 K is 3.9 $W\,m^{-1}\,K^{-1}$. For Bi_2Se_3, the measured bulk κ_l value at 300 K is 2 $W\,m^{-1}\,K^{-1}$.[75,80] A value of 2000 $W\,m^{-1}\,K^{-1}$ is

TABLE I. Calculated and experimental properties of bulk Mexican-hat materials GaS, GaSe, InS, InSe, Bi_2Se_3, bilayer graphe(BLG), and Bi(111). The in-plane and c-axis lattice constants are a_0 and c_0, respectively. The thickness of an individual layer is *d*, and the van-der-Waal distance between individual monolayers is d_{vdW}. The calculated thickness, *d*, is the atom-center to atom-center distance between the top and bottom chalcogen atoms of a single layer in GaS, GaSe, InS, InSe, Bi_2Se_3, and atom center to atom center distance of the top and bottom carbon atoms in bilayer graphene. The thickness *d* in monolayer Bi is the height of the buckling distance between the two Bi atoms. Experimental values when available[16,65–69] are included for comparison.

	a_0 (Å)	c_0 (Å)	*d* (Å)	d_{vdW} (Å)	a_0^{expt} (Å)	c_0^{expt} (Å)	d^{expt} (Å)
GaS	3.630	15.701	4.666	3.184	3.587	15.492	4.599
GaSe	3.755	15.898	4.870	3.079	3.752	15.950	4.941
InS	3.818	15.942	5.193	2.780	…	…	…
InSe	4.028	16.907	5.412	3.040	4.000	16.640	5.557
Bi_2Se_3	4.140	28.732	7.412	3.320	4.143	28.636	…
BLG	2.459	…	3.349	3.349	2.460	…	3.400
Bi(111)	4.34	…	3.049	…	4.54	…	…

used for the room temperature in-plane lattice thermal conductivity of bilayer graphene. This is consistent with a number of experimental measurements and theoretical predictions on the lattice thermal conductivity of bilayer graphene.[81,82] Prior studies of thermal conductivity in the layered chalcogenides and few layer graphene have demonstrated that κ_l can vary by up to a factor of 2 as the film thickness decreases from bulk to a monolayer.[83–86] Maximum and minimum values for ZT are estimated for GaS, GaSe, InS, InSe, and Bi_2Se_3 using the bulk values of κ_l and twice the bulk values of κ_l.

When evaluating *ZT* in Eq. (6) for the 2D thin film structures, the bulk lattice thermal conductivity is multiplied by the film thickness. When tabulating values of the electrical conductivity and the power factor of the 2D films, the calculated conductivity from Eq. (1) is divided by the film thickness.

Much of the experimental data from which the values for λ_0 and κ_l have been determined are from bulk studies, and clearly these values might change as the materials are thinned down to a few monolayers. However, there are presently no experimental values available for few-layer III–VI and Bi_2Se_3 materials. Our primary objective is to obtain a qualitative understanding of the effect of bandstructure in these materials on their thermoelectric properties. To do so, we use the above values for λ_0 and κ_l to estimate *ZT* for each material as a function of thickness. We tabulate these values and provide the corresponding values for the electron or hole density, Seebeck coefficient, and conductivity at maximum *ZT*. It is clear from Eqs. (3) and (4) that the Seebeck coefficient is relatively insensitive to the value of the mean free path. Therefore, if more accurate values for the conductivity or κ_l become available, new values for *ZT* can be estimated from Eq. (6) using the given Seebeck coefficient and replacing the electrical and/or thermal conductivity.

III. NUMERICAL RESULTS

A. III-VI compounds GaX and InX (X = S, Se)

The lattice parameters of the optimized bulk GaX and InX compounds are summarized in Table I. In this study, the default stacking is the β phase illustrated in Fig. 2(a). The β phase is isostructural to the AA′ stacking order in the 2H polytypes of the molybdenum and tungsten dichalcogenides.[87] The bandgap of the one to four monolayer structures is indirect for GaS, GaSe, InS, and InSe. Figure 3 illustrates the PBE band structure for one-layer (1L) through four-layers (4L), eight-layer (8L), and bulk GaS. The PBE SOC band gaps and energy transitions for each of the III–VI materials and film thicknesses are listed in Table II. For GaS, the HSE SOC values are also listed. The effective masses extracted from the PBE SOC electronic bandstructure are listed in Table III.

The conduction band minimum of GaSe, InS, and InSe is at Γ for all layer thicknesses, from monolayer to bulk. The conduction band minimum of monolayer GaS is at M. This result is consistent with that of Zólyomi *et al.*[3] However, for all thicknesses greater than a monolayer, the conduction band of GaS is at Γ. Results from the PBE functional give GaS conduction valley separations between M and Γ that are on the order of k_BT at room temperature, and this leads to qualitatively incorrect results in the calculation of the electronic and thermoelectric parameters. For the three other III–VI compounds, the minimum PBE-SOC spacing between the conduction Γ and M valleys is 138 meV in monolayer GaSe. For InS and InSe, the minimum conduction Γ-M valley separations also occur for a monolayer, and they are 416 eV and 628 eV, respectively. For monolayer GaS, the HSE-SOC conduction M valley lies 80 meV below the K valley and 285 meV below the Γ valley. At two to four layer thicknesses, the order is reversed, the conduction band edge

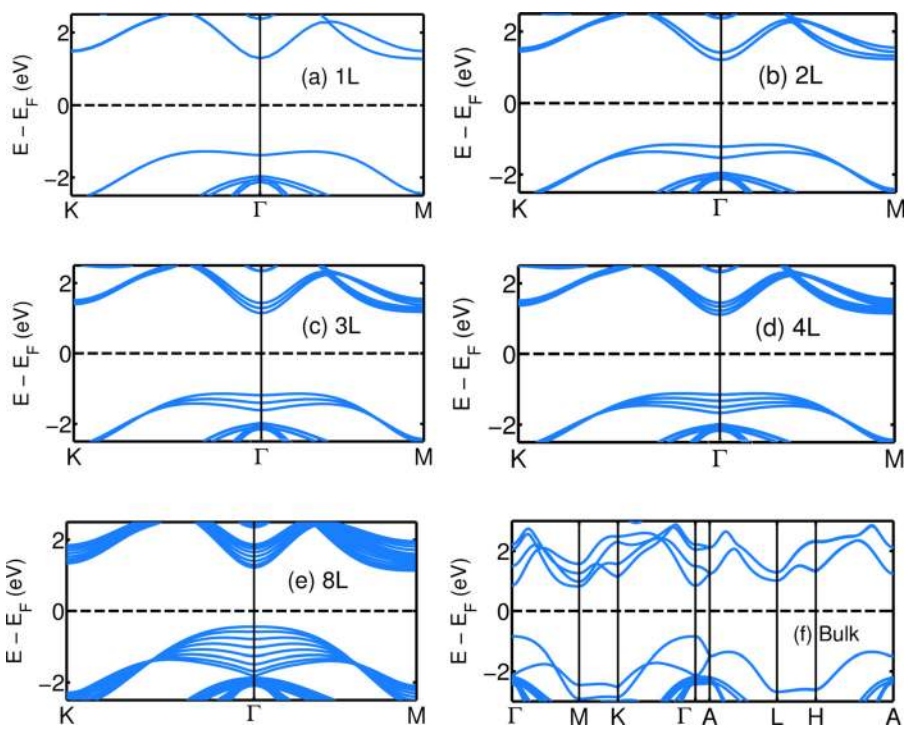

FIG. 3. PBE SOC band structure of GaS: (a) 1L, (b) 2L, (c) 3L, (d) 4L, (e) 8L, and (f) bulk GaS.

TABLE II. PBE SOC calculations of the bandgap energies and energy transitions between the valence band edge of the Mexican hat band (E_v) and the conduction (c) band valleys for 1L to 4L GaS, GaSe, InS, and InSe. The bandgap at each dimension is highlighted in bold text. The HSE-SOC energy transitions for GaS are in parentheses.

Structure	Transition	GaS	GaSe	InS	InSe
1L	E_v to Γ_c	2.563 (3.707)	**2.145**	**2.104**	**1.618**
	E_v to K_c	2.769 (3.502)	2.598	2.684	2.551
	E_v to M_c	**2.549 (3.422)**	2.283	2.520	2.246
2L	E_v to Γ_c	**2.369 (3.156)**	**1.894**	**1.888**	**1.332**
	E_v to K_c	2.606 (3.454)	2.389	2.567	2.340
	E_v to M_c	2.389 (3.406)	2.065	2.353	2.025
3L	E_v to Γ_c	**2.288 (3.089)**	**1.782**	**1.789**	**1.152**
	E_v to K_c	2.543 (3.408)	2.302	2.496	2.201
	E_v to M_c	2.321 (3.352)	1.967	2.273	1.867
4L	E_v to Γ_c	**2.228 (3.011)**	**1.689**	**1.749**	**1.086**
	E_v to K_c	2.496 (3.392)	2.224	2.471	2.085
	E_v to M_c	2.267 (3.321)	1.879	2.242	1.785
Bulk	Γ_v to Γ_c	1.691 (2.705)	**0.869**	**0.949**	**0.399**
	Γ_v to K_c	1.983 (2.582)	1.435	1.734	1.584
	Γ_v to M_c	**1.667 (2.391)**	0.964	1.400	1.120

is at Γ, and the energy differences between the valleys increase. For the electronic and thermoelectric properties, only energies within a few k_BT of the band edges are important. Therefore, the density of modes of n-type GaS is calculated from the HSE-SOC bandstructure. For p-type GaS and all other materials, the densities of modes are calculated from the PBE-SOC bandstructure.

The orbital composition of the monolayer GaS conduction Γ valley contains 63% Ga s orbitals and 21% S p_z orbitals. The orbital compositions of the other III-VI conduction Γ valleys are similar. As the film thickness increases from a monolayer to a bilayer, the conduction Γ valleys in each layer couple and split by 203 meV as shown in Fig. 3(b). Thus, as the film thickness increases, the number of low-energy Γ states near the conduction band-edge remains the same, or, saying it another way, the number of low-energy Γ states per unit thickness decreases by a factor of two as the number of layers increases from a monolayer to a bilayer. This affects the electronic and thermoelectric properties.

The Mexican hat feature of the valence band is present in all of the 1L-4L GaX and InX structures, and it is most pronounced for the monolayer structure shown in Fig. 3(a). For monolayer GaS, the highest valence band at Γ is composed of 79% sulfur p_z orbitals (p_z^S). The lower 4 valence bands at Γ are composed entirely of sulfur p_x and p_y orbitals (p_{xy}^S). When multiple layers are brought together, the p_z^S valence band at Γ strongly couples and splits with a splitting of 307 meV in the bilayer. For the 8-layer structure in Fig. 3(e), the manifold of 8 p_z^S bands touches the manifold of p_{xy}^S bands, and the bandstructure is bulklike with discrete k_z momenta. In the bulk shown in Fig. 3(f), the discrete energies become a continuous dispersion from Γ to A. At 8 layer thickness, the large splitting of the p_z^S valence band removes the Mexican hat feature, and the valence band edge is parabolic as in the bulk. The nature and orbital composition of the bands of the 4 III–VI compounds are qualitatively the same.

TABLE IV. Values of ϵ_0 and k_0 are listed in order of thicknesses: 1L, 2L, 3L, and 4L. The default level of theory is PBE with spin-orbit coupling, and the default stacking is AA′. Only deviations from the defaults are noted.

Material (Theory/stacking order)	ϵ_0 (meV) 1L, 2L, 3L, 4L	k_0 (nm^{-1}) 1L, 2L, 3L, 4L
GaS	111.2, 59.6, 43.8, 33.0	3.68, 2.73, 2.52, 2.32
GaS (no-SOC)	108.3, 60.9, 45.1, 34.1	3.16, 2.63, 2.32, 2.12
GaS (HSE)	97.9, 50.3, 40.9, 31.6	2.81, 2.39, 2.08, 1.75
GaS (AA)	111.2, 71.5, 57.1, 47.4	3.68, 2.93, 2.73, 2.49
GaSe	58.7, 29.3, 18.1, 10.3	2.64, 2.34, 1.66, 1.56
GaSe (ϵ)	58.7, 41.2, 23.7, 5.1	2.64, 1.76, 1.17, 1.01
InS	100.6, 44.7, 25.8, 20.4	4.03, 3.07, 2.69, 2.39
InSe	34.9, 11.9, 5.1, 6.1	2.55, 1.73, 1.27, 1.36
InSe (HSE)	38.2, 15.2, 8.6, 9.2	2.72, 2.20, 1.97, 2.04
Bi_2Se_3	314.7, 62.3, 12.4, 10.4	3.86, 1.23, 1.05, 0.88
Bi_2Se_3 (no-SOC)	350.5, 74.6, 22.8, 20.1	4.19, 1.47, 1.07, 1.02

In the few-layer structures, the Mexican hat feature of the valence band can be characterized by the height, ϵ_0, at Γ and the radius of the band-edge ring, k_0, as illustrated in Figure 2(b). The actual ring has a small anisotropy that has been previously characterized and discussed in detail.[3,4,13] For all four III–VI compounds of monolayer and few-layer thicknesses, the valence band maximum (VBM) of the inverted Mexican hat lies along $\Gamma - K$, and it is slightly higher in energy compared to the band extremum along $\Gamma - M$. In monolayer GaS, the valence band maximum along $\Gamma - K$ is 4.7 meV above the band extremum along $\Gamma - M$. In GaS, as the film thickness increases from one layer to four layers the energy difference between the two extrema decreases from 4.7 meV to 0.41 meV. The maximum energy difference of 6.6 meV between the band extrema of the Mexican hat occurs in a monolayer of InS. The tabulated values of k_0 in Table IV give the distance from Γ to the VBM in the $\Gamma - K$ direction. Results calculated from PBE and HSE functionals are given, and results with and without spin-orbit coupling are listed. The effects of AA′ versus AA stacking

TABLE III. *Ab-initio* calculations of the hole and electron effective masses at the Γ valley of the valence band and conduction band, respectively, for each structure in units of the free electron mass (m_0). The conduction band effective masses at M_c are included in parentheses for one to four layers of GaS.

	GaS	GaSe	InS	InSe	GaS	GaSe	InS	InSe
Structure	Hole effective mass (m_0)				Electron effective mass (m_0)			
1L	0.409	0.544	0.602	0.912	0.067 (0.698)	0.053	0.080	0.060
2L	0.600	0.906	0.930	1.874	0.065 (0.699)	0.051	0.075	0.055
3L	0.746	1.439	1.329	6.260	0.064 (0.711)	0.050	0.074	0.053
4L	0.926	2.857	1.550	3.611	0.064 (0.716)	0.049	0.073	0.055

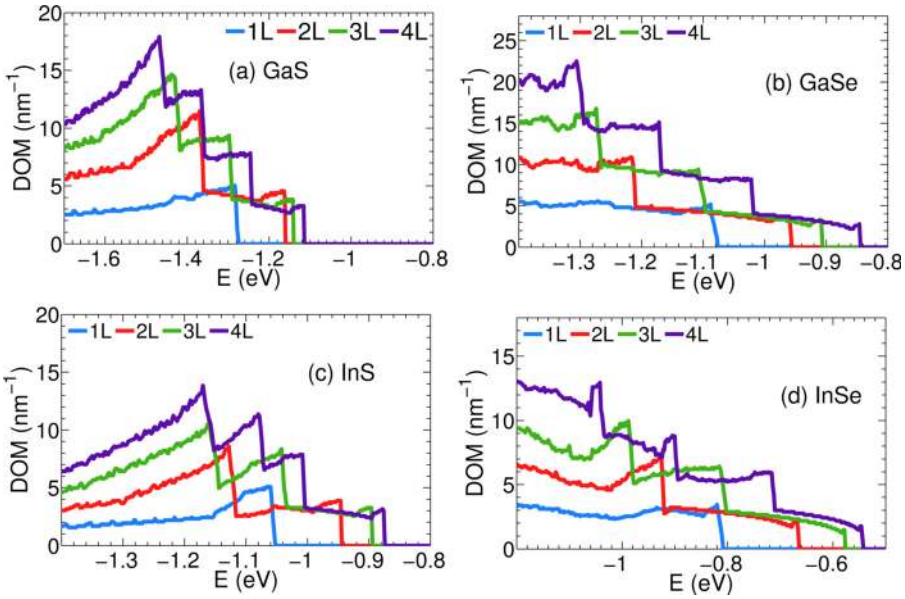

FIG. 4. Distribution of valence band modes per unit width versus energy for (a) GaS, (b) GaSe, (c) InS, and (d) InSe for 1L (blue), 2L (red), 3L (green), and 4L (purple) structures. The midgap energy is set to E = 0.

order of GaS and AA′ versus ϵ stacking order of GaSe[88,89] are also compared.

Table IV shows that the valence band Mexican hat feature is robust. It is little affected by the choice of functional, the omission or inclusion of spin-orbit coupling, or the stacking order. A recent study of GaSe at the G_0W_0 level found that the Mexican hat feature is also robust against many-electron self-energy effects.[13] For all materials, the values of ϵ_0 and k_0 are largest for monolayers and decrease as the film thicknesses increase. This suggests that the height of the step function density of modes will also be maximum for the monolayer structures.

Figure 4 illustrates the valence band density of modes for 1L, 2L, 3L, and 4L for GaS, GaSe, InS, and InSe. The valence band density of modes is a step function for the few-layer structures. The height of the step function for monolayer GaS, GaSe, InS, and InSe is 4.8 nm^{-1}, 5.2 nm^{-1}, 5.1 nm^{-1}, and 3.4 nm^{-1}, respectively. The height of the density of modes in GaS decreases by ∼30% when the film thickness increases from one to four monolayers. For all four materials GaS, GaSe, InS, and InSe, decreasing the film thickness increases k_0 and the height of the step-function of the band-edge density of modes.

The p-type Seebeck coefficients, the p- and n-type power factors, and the thermoelectric figures-of-merit (ZT) as functions of carrier concentration at room temperature for GaS, GaSe, InS, and InSe are shown in Figure 5. The thermoelectric parameters at $T = 300$ K of bulk and one to four monolayers of GaS, GaSe, InS, and InSe are summarized in Tables V–VIII. For each material, the peak p-type ZT occurs

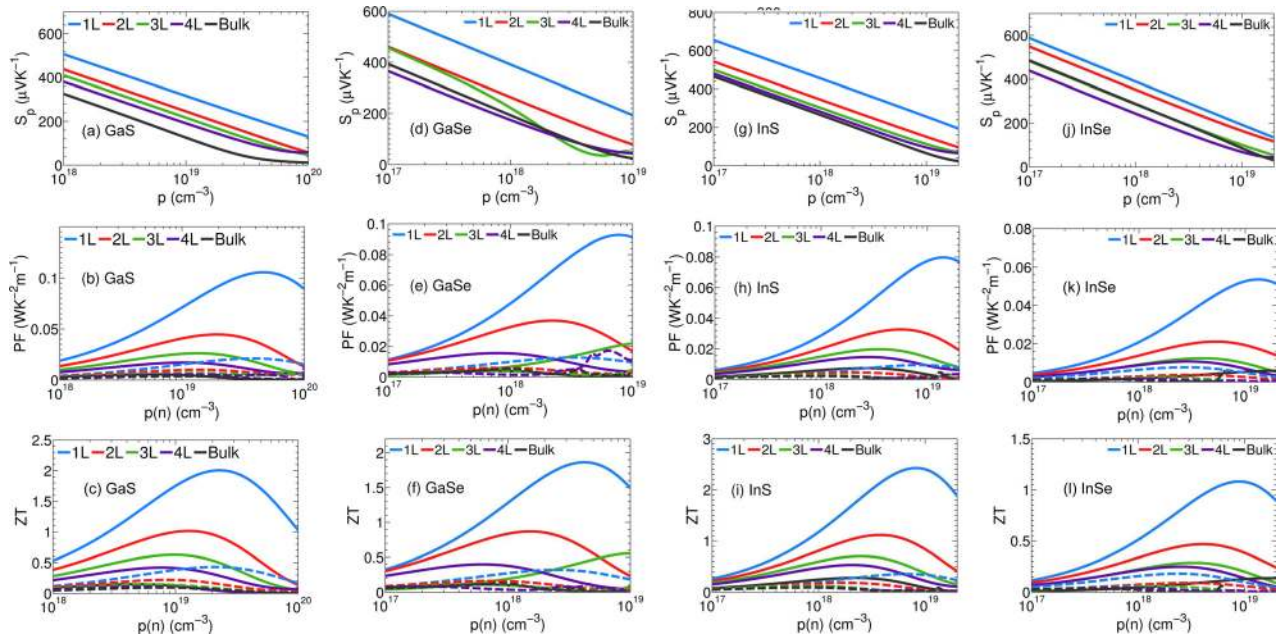

FIG. 5. Seebeck coefficient, power factor and thermoelectric figure-of-merit, ZT, of p-type (solid line) and n-type (broken line) 1L (blue), 2L (red), 3L (green), 4L (purple), and bulk (black) for (a)–(c) GaS, (d)–(f) GaSe, (g)–(i) InS, and (j)–(l) InSe at room temperature.

TABLE V. GaS thermoelectric properties for bulk and one to four monolayers at $T = 300$ K. Hole and electron carrier concentrations (p and n), Seebeck coefficients (S_p and S_e), and electrical conductivities (σ_p and σ_n) at the peak p- and n-type ZT. The maximum and minimum ZT are listed for two different approximations of κ_l, the minimum ZT is listed in parentheses. The thermoelectric parameters are computed using an electron and hole mean free path, $\lambda = 25$ nm and a lattice thermal conductivity, κ_l, of 10 W m^{-1} K^{-1} for the maximum ZT and 20 W m^{-1} K^{-1} for the minimum ZT.

Thickness	p (10^{19} cm^{-3})	S_p (μV K^{-1})	σ_p ($10^6\Omega$ m)$^{-1}$	ZT_p	n (10^{19} cm^{-3})	$\lvert -S_e \rvert$ (μV K^{-1})	σ_e ($10^6\Omega$ m)$^{-1}$	ZT_e
1L	3.19	251.6	1.41	2.01 (1.42)	1.02	237.0	0.348	0.431 (0.620)
2L	1.51	222.9	0.776	1.02 (0.641)	0.621	219.6	0.229	0.218 (0.362)
3L	1.13	213.2	0.530	0.630 (0.412)	0.595	200.9	0.206	0.147 (0.273)
4L	0.922	211.2	0.390	0.421 (0.290)	0.545	191.9	0.195	0.111 (0.231)
Bulk	0.330	187.6	0.149	0.140	0.374	210.8	0.116	0.095

TABLE VI. GaSe thermoelectric properties for bulk and one to four monolayers at 300 K. Hole and electron carrier concentrations (p and n), Seebeck coefficients (S_p and S_e), and electrical conductivities (σ_p and σ_n) at the peak p- and n-type ZT. The maximum and minimum ZT are listed for two different approximations of κ_l, the minimum ZT is listed in parentheses. The thermoelectric parameters are computed using an electron and hole mean free path, $\lambda = 25$ nm and a lattice thermal conductivity, κ_l, of 10 W m^{-1} K^{-1} for the maximum ZT and 20 W m^{-1} K^{-1} for the minimum ZT.

Thickness	p (10^{18} cm^{-3})	S_p (μV K^{-1})	σ_p (Ω m)$^{-1}$	ZT_p	n (10^{18} cm^{-3})	$\lvert -S_e \rvert$ (μV K^{-1})	σ_e ($10^6\Omega$ m)$^{-1}$	ZT_e
1L	5.81	256.1	1.28	1.86 (1.07)	2.71	202.9	0.310	0.321 (0.172)
2L	2.70	225.3	0.711	0.870 (0.471)	1.20	201.4	0.152	0.162 (0.081)
3L	2.09	221.2	0.450	0.561 (0.293)	0.79	194.0	0.103	0.110 (0.054)
4L	1.49	210.2	0.352	0.391 (0.211)	0.69	186.4	0.085	0.082 (0.041)
Bulk	0.541	180.9	0.121	0.112	0.29	127.9	0.033	0.132

TABLE VII. InS thermoelectric properties for bulk and one to four monolayers at $T = 300$ K. Hole and electron carrier concentrations (p and n), Seebeck coefficients (S_p and S_e), and electrical conductivities (σ_p and σ_n) at the peak p- and n-type ZT. The maximum and minimum ZT are listed for two different approximations of κ_l, the minimum ZT is listed in parentheses. The thermoelectric parameters are computed using an electron and hole mean free path, $\lambda = 25$ nm and a lattice thermal conductivity, κ_l, of 7.1 W m^{-1} K^{-1} for the maximum ZT and 14.2 W m^{-1} K^{-1} for the minimum ZT.

Thickness	p (10^{18} cm^{-3})	S_p (μV K^{-1})	σ_p ($10^6\Omega$ m)$^{-1}$	ZT_p	n (10^{18} cm^{-3})	$\lvert -S_e \rvert$ (μV K^{-1})	σ_e ($10^6\Omega$ m)$^{-1}$	ZT_e
1L	9.30	244.2	1.26	2.43 (1.38)	3.75	210.8	0.210	0.350 (0.191)
2L	4.20	228.7	0.610	1.12 (0.612)	1.63	200.0	0.113	0.181 (0.093)
3L	2.32	229.5	0.361	0.701 (0.383)	1.25	196.9	0.078	0.120 (0.062)
4L	1.91	222.0	0.292	0.532 (0.281)	1.02	198.1	0.059	0.094 (0.048)
Bulk	1.30	195.1	0.180	0.280	1.21	179.8	0.070	0.092

TABLE VIII. InSe thermoelectric properties for bulk and one to four monolayers at $T = 300$ K. Hole and electron carrier concentrations (p and n), Seebeck coefficients (S_p and S_e), and electrical conductivities (σ_p and σ_n) at the peak p- and n-type ZT. The maximum and minimum ZT are listed for two different approximations of κ_l, the minimum ZT is listed in parentheses. The thermoelectric parameters are computed using an electron and hole mean free path, $\lambda = 25$ nm and a lattice thermal conductivity, κ_l, of 12 W m^{-1} K^{-1} for the maximum ZT and 24 W m^{-1} K^{-1} for the minimum ZT.

Thickness	p (10^{18} cm^{-3})	S_p (μV K^{-1})	σ_p ($10^6\Omega$ m)$^{-1}$	ZT_p	n (10^{18} cm^{-3})	$\lvert -S_e \rvert$ (μV K^{-1})	σ_e ($10^6\Omega$ m)$^{-1}$	ZT_e
1L	9.71	229.8	0.981	1.08 (0.592)	2.34	200.5	0.192	0.180 (0.092)
2L	4.04	219.8	0.430	0.471 (0.251)	1.22	194.7	0.111	0.090 (0.046)
3L	4.18	204.2	0.471	0.292 (0.150)	0.781	189.1	0.067	0.059 (0.029)
4L	2.45	201.0	0.261	0.252 (0.131)	0.610	186.8	0.053	0.045 (0.023)
Bulk	1.75	179.1	0.181	0.142	0.652	160.9	0.054	0.034

at a monolayer thickness. The largest room temperature p-type ZT occurs in monolayer InS. At room temperature, the peak p-type (n-type) ZT values in 1L, 2L, 3L, and 4L GaS occur when the Fermi level is 42 meV, 38 meV, 34 meV, and 30 meV (22 meV, 17 meV, 11 meV, and 7 meV) above (below) the valence (conduction) band edge, and the Fermi level positions in GaSe, InS, and InSe change in qualitatively the same way. The p-type hole concentrations of monolayer GaS, GaSe, InS, and InSe at the peak ZT are enhanced by factors of 9.7, 10.8, 7.2, and 5.5 compared to those of their respective bulk structures. At the peak p-type room-temperature ZT, the Seebeck coefficients of monolayer GaS, GaSe, InS, and InSe are enhanced by factors of 1.3, 1.4, 1.3, and 1.3, respectively, compared to their bulk values.

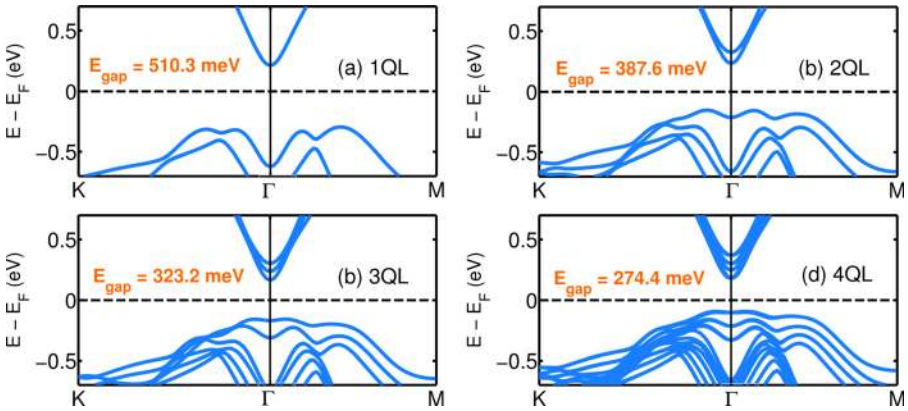

FIG. 6. *Ab-initio* band structure including spin-orbit interaction of Bi_2Se_3: (a) 1 QL, (b) 2 QL, (c) 3 QL, and (d) 4 QL.

However, the monolayer and bulk peak ZT values occur at carrier concentrations that differ by an order of magnitude. The p-type power factor (PF) at the peak ZT for 1L GaS is enhanced by a factor of 17 compared to that of bulk GaS. Assuming the same κ_l for the bulk and few-layer structures, the p-type ZT values of monolayer GaS, GaSe, InS, and InSe are enhanced by factors of 14, 17, 9, and 8, respectively, compared to their bulk values. At the peak p-type ZT, the contribution of κ_e to κ_{tot} is minimum for the bulk structure and maximum for the monolayer structure. The contributions of κ_e to κ_{tot} in bulk and monolayer GaS are 5% and 24%, respectively. The increasing contribution of κ_e to κ_{tot} with decreasing film thickness reduces the enhancement of ZT relative to that of the power factor.

While the focus of the paper is on the effect of the Mexican hat dispersion that forms in the valence band of these materials, the n-type thermoelectric figure of merit also increases as the film thickness is reduced to a few layers, and it is also maximum at monolayer thickness. The room temperature, monolayer, n-type thermoelectric figures of merit of GaS, GaSe, InS, and InSe are enhanced by factors of 4.5, 2.4, 3.8, and 5.3, respectively, compared to the those of the respective bulk structures. The largest n-type ZT occurs in monolayer GaS. In a GaS monolayer, the 3-fold degenerate M valleys form the conduction band edge. This large valley degeneracy gives GaS the largest n-type ZT among the 4 III-VI compounds. As the GaS film thickness increases from a monolayer to a bilayer, the conduction band edge moves to the non-degenerate Γ valley so that the number of low-energy states near the conduction band edge decreases. With an added third and fourth layer, the M valleys move higher, and the Γ valley continues to split so that the number of low-energy conduction states does not increase with film thickness. Thus, for a Fermi energy fixed slightly below the band edge, the electron density and the conductivity decrease as the number of layers increase as shown in Tables V–VIII. As a result, the maximum n-type ZT for each material occurs at a single monolayer and decreases with each additional layer.

B. Bi_2Se_3

Bi_2Se_3 is an iso-structural compound of the well known thermoelectric, Bi_2Te_3. Both materials have been intensely studied recently because they are also topological insulators.[90–92] Bulk Bi_2Se_3 has been studied less for its thermoelectric properties due to its slightly higher thermal conductivity compared to Bi_2Te_3. The bulk thermal conductivity of Bi_2Se_3 is 2 W-(m K)$^{-1}$ compared to a bulk thermal conductivity of 1.5 W-(m K)$^{-1}$ reported for Bi_2Te_3.[80,93] However, the thermoelectric performance of bulk Bi_2Te_3 is limited to a narrow temperature window around room temperature because of its small bulk band gap of approximately 160 meV.[90] The band gap of single quintuple layer (QL) Bi_2Te_3 was previously calculated to be 190 meV.[21] In contrast, the bulk bandgap of Bi_2Se_3 is ~300 meV (Ref. 94) which allows it to be utilized at higher temperatures.

The optimized lattice parameters for bulk Bi_2Se_3 are listed in Table I. The optimized bulk crystal structure and bulk band gap are consistent with prior experimental and theoretical studies of bulk Bi_2Se_3.[22,68] Using the optimized lattice parameters of the bulk structure, the electronic structures of one to four quintuple layers of Bi_2Se_3 are calculated with the inclusion of spin-orbit coupling. The electronic structures of 1 to 4 QLs of Bi_2Se_3 are shown in Figure 6. The band gaps for one to four quintuple layers of Bi_2Se_3 are 510 meV, 388 meV, 323 meV, and 274 meV for the 1QL, 2QL, 3QL, and 4QL films, respectively. The gapping of the surface states in few-layer Bi_2Se_3 is consistent with experimental data[95] and other *ab-initio* calculations.[22,96]

The effective masses of the conduction and valence band at Γ for 1QL to 4QL of Bi_2Se_3 are listed in Table IX. For each of the thin film structures, the conduction bands are parabolic and located at Γ. The conduction band at Γ of the 1QL structure is composed of 13% Se *s*, 24% Se p_{xy}, 16% Bi p_{xy}, and 39% Bi p_z. The orbital composition of the Γ valley remains qualitatively the same as the film thickness increases to 4QL. The orbital composition of the bulk conduction band is 79% Se p_z and 16% Bi *s*. As the film thickness increases above 1QL, the conduction band at Γ splits, as illustrated in Figs. 6(b)–6(d). In the 2QL, 3QL, and 4QL structures, the

TABLE IX. *Ab-initio* calculations of the hole and electron effective masses at the Γ-valley valence and conduction band edges of Bi_2Se_2.

Structure	Γ_v (m_0)	Γ_c (m_0)
1L	0.128	0.132
2L	0.436	0.115
3L	1.435	0.176
4L	1.853	0.126

conduction band splitting varies between 53.9 meV and 88.2 meV. As with the III–VIs, the number of low-energy conduction band states per unit thickness decreases with increasing thickness.

The valence bands have slightly anistropic Mexican hat dispersions. The values of ϵ_0 and k_0 used to characterize the Mexican hat for the 1QL to 4QL structures of Bi_2Se_3 are listed in Table IV. The radius k_0 is the distance from Γ_v to the band extremum along $\Gamma_v - M_v$, which is the valence band maxima for the 1QL to 4QL structures. The energy difference between the valence band maxima and the band extremum along $\Gamma_v - K_v$ decreases from 19.2 meV to 0.56 meV as the film thickness increases from 1QL to 4QL. The Mexican hat dispersion in 1QL of Bi_2Se_3 is better described as a double brimmed hat consisting of two concentric rings in k-space characterized by four points of extrema that are nearly degenerate. The band extremum along $\Gamma_v - M_v$ adjacent to the valence band maxima is 36 meV below the valence band maxima. Along $\Gamma_v - K_v$, the energy difference between the two band extrema is 4.2 meV. At Γ_v, the orbital composition of the valence band for 1QL of Bi_2Se_3 is 63% p_z orbitals of Se, 11% p_{xy} orbitals of Se, and 18% s orbitals of Bi, and the orbital composition remains qualitatively the same as the film thickness increases to 4QL. As the thickness increases above a monolayer, the energy splitting of the valence bands from each layer is large with respect to room temperature k_BT and more complex than the splitting seen in the III–VIs. At a bilayer, the highest valence band loses most of the outer k-space ring, the radius k_0 decreases by a factor 3.1, and the height (ϵ_0) of the hat decreases by a factor of 5.1. This decrease translates into a decrease in the initial step height of the density of modes shown in Figure 7(a). The second highest valence band retains most of the shape of the original monolayer valence band, but it is now too far from the valence band edge to contribute to the low-energy electronic or thermoelectric properties. Thus, Bi_2Se_3 follows the same trends as seen in Bi_2Te_3; the large enhancement in the thermoelectric properties resulting from bandstructure is only significant for a monolayer.[50] Assuming the same κ_l for the bulk and single quintuple layer structure, the p-type ZT for the single quintuple layer is enhanced by a factor of 4.3 compared to that of the bulk film. At the peak ZT, the hole concentration is 4 times larger than that of the bulk, and the position of the Fermi energy with respect to the valence band edge ($E_F - E_V$) is 45 meV higher than that of the bulk.

The peak room temperature n-type ZT also occurs for 1QL of Bi_2Se_3. In one to four quintuple layers of Bi_2Se_3, two degenerate bands at Γ contribute to the conduction band density of modes. The higher Γ valleys contribute little to the conductivity as the film thickness increases. The Fermi levels at the peak n-type, room-temperature ZT rise from 34 meV to 12 meV below the conduction band edge as the film thickness increases from 1 QL to 4 QL, while the electron density decreases by a factor of 1.8. This results in a maximum n-type ZT for the 1QL structure.

The p- and n-type Seebeck coefficient, electrical conductivity, power factor, and the thermoelectric figure-of-merit (ZT) as a function of carrier concentration at room temperature for Bi_2Se_3 are illustrated in Figure 7. The thermoelectric parameters at $T = 300$ K of bulk and one to four quintuple layers for Bi_2Se_3 are summarized in Table X.

There have been several prior studies of the thermoelectric properties of single and few quintuple layer Bi_2Se_3, and it is useful to make comparisons to understand the differences and similarities. Saeed *et al.*[22] calculated a p-type ZT value of 0.27 and a p-type peak power factor of 0.432 mW m^{-1} K^{-2} for 1QL of Bi_2Se_3 using *ab initio* band structure, a hole relaxation time of 2.7 fs, and a thermal conductivity of 0.49 W/mK.

The disparity between their values and ours result from the different approximations made for the relaxation time (2.7 fs) and lattice thermal conductivity (0.49 W/mK). To reproduce their results, we convert the relaxation time of 2.7 fs into a mean free path of 0.27 nm, using an average thermal velocity of 10^5 m/s determined from the 1QL valence bandstructure. This hole mean free path is approximately 2/3 of the in-plane lattice constant which pushes the limits of validity of the semiclassical Boltzmann transport approach. Using

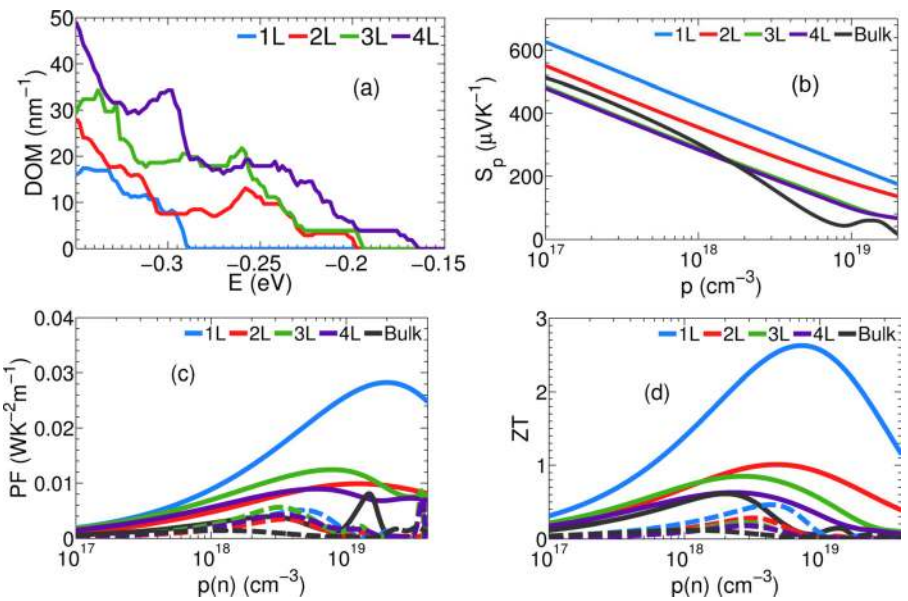

FIG. 7. (a) Distribution of modes per unit width versus energy for Bi_2Se_3. The midgap energy is set to E = 0. Thermoelectric properties of p-type (solid line) and n-type (broken line) Bi_2Se_3: (b) Seebeck coefficient, (c) power factor, and (d) thermoelectric figure-of-merit, ZT, at room temperature for 1L (blue), 2L (red), 3L (green), 4L (purple), and bulk (black).

TABLE X. Bi_2Se_3 thermoelectric properties for bulk and one to four quintuple layers at $T = 300$ K. Hole and electron carrier concentrations (p and n), Seebeck coefficients (S_p and S_e), and electrical conductivities (σ_p and σ_n) at the peak p- and n-type ZT. The maximum and minimum ZT are listed for two different approximations of κ_l, the minimum ZT is listed in parentheses. The thermoelectric parameters are computed using an electron mean free path, λ_e of 5.1 nm and hole mean free path, $\lambda_p = 2.1$ nm and a lattice thermal conductivity, κ_l, of 2 W m^{-1} K^{-1} for the maximum ZT and 4 W m^{-1} K^{-1} for the minimum ZT.

Thickness	p (10^{18} cm^{-3})	S_p (μV K^{-1})	σ_p ($10^6\Omega$ m)$^{-1}$	ZT_p	n (10^{18} cm^{-3})	$\lvert -S_e \rvert$ (μV K^{-1})	σ_e ($10^6\Omega$ m)$^{-1}$	ZT_e
1L	7.66	279.3	0.321	2.62 (1.76)	4.63	210.1	0.112	0.463 (0.249)
2L	4.65	251.3	0.245	1.07 (0.691)	3.38	208.2	0.081	0.280 (0.182)
3L	2.77	259.4	0.152	0.791 (0.622)	2.96	198.3	0.071	0.218 (0.120)
4L	2.58	237.8	0.141	0.624 (0.561)	2.56	185.8	0.062	0.176 (0.081)
Bulk	1.95	210.7	0.085	0.610	1.23	191.9	0.033	0.129

the hole mean free path of 0.27 nm and the lattice thermal conductivity of 0.49 W/m K, our calculation gives a peak p-type ZT of 0.28 and peak p-type power factor of 0.302 mW m^{-1} K^{-2}, which agrees well with the results in Ref. 22.

C. Bilayer graphene

AB stacked bilayer graphene(BLG) is a gapless semiconductor with parabolic conduction and valence bands that are located at the K (K') symmetry points. Prior experimental[6,97] and theoretical[23] studies demonstrated the formation of a bandgap in BLG with the application of a vertical electric field. The vertical electric field also deforms the conduction and valence band edges at K into a Mexican-hat dispersion.[2,6] Using *ab-initio* calculations, we compute the band structure of bilayer graphene subject to vertical electric fields ranging from 0.1 V/nm to 1 V/nm. The lattice parameters for the bilayer graphene structure used in our simulation are given in Table I. The *ab-initio* calculated band gaps are in good agreement with prior calculations.[23,98] The bandgap increases from 31.4 meV to 223.1 meV as the applied field increases from 0.1 V/nm to 1 V/nm.

For each applied field ranging from 0.1 V/nm to 1 V/nm, both the valence band and the conduction band edges lie along the path $\Gamma - K$, and the radius k_0 is the distance from K to the band edge along $\Gamma - K$. The magnitude of k_0 increases approximately linearly with the electric field as shown in Figure 8(a). The dispersions of the valence band and the conduction band quantitatively differ, and k_0 of the valence band is up to 10% larger than k_0 of the conduction band. The anisotropy of the conduction and valence Mexican hat dispersions increases with increasing vertical field. The extremum point along K–M of the valence (conduction) band Mexican hat dispersion is lower (higher) in energy compared to the band extremum along $\Gamma - K$. As the field increases from 0.1 V/nm to 1.0 V/nm, the energy difference between the two extrema points increases from 1.2 meV to 21.6 meV in the valence band and 3.7 meV to 30.1 meV in the conduction band. This anisotropy in the Mexican hat of the valence and conduction band leads to a finite slope in the density of modes illustrated in Figure 8(b).

As the applied field is increased from 0.1 V/nm to 1.0 V/nm, the height of the density of modes step function in the valence and conduction band increases by a factor of 2.6 as illustrated in Fig. 8(b). Even though the bandgap increases with bias, at a fixed Fermi level, the charge density also increases with bias. For Fermi energies within the bandgap, the energy per carrier, with respect to the Fermi energy, also increases resulting in an increase in the Seebeck coefficient shown in Fig. 8(c). The increase in the Seebeck coefficient and the charge density leads to the increase in ZT shown in Fig. 8(d). For an applied electric field of 1 V/nm, the p- and n-type ZT are enhanced by a factor of 2.8 and 2.6 in bilayer graphene compared to the ZT of bilayer graphene with no applied electric field. The p-type thermoelectric parameters

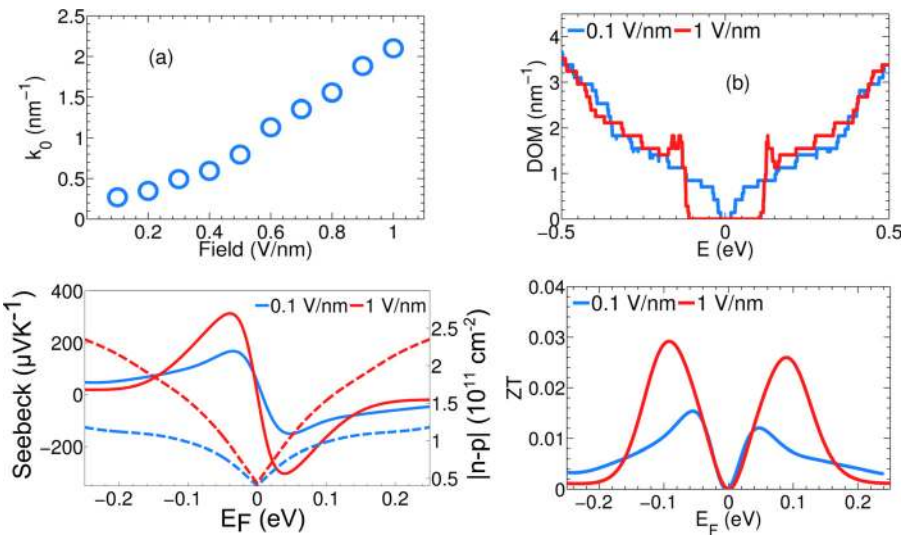

FIG. 8. (a) Evolution of the radius k_0 of the Mexican hat in bilayer graphene as a function of an applied vertical electric field. (b) Density of modes per unit width for two different vertical fields of 0.1 V/nm (blue) and 1 V/nm (red). (c) Seebeck coefficients (solid lines) and carrier concentrations (broken lines) for two different vertical fields. (d) ZT of bilayer graphene as a function of the Fermi level for two different vertical fields.

TABLE XI. Bilayer graphene p-type thermoelectric properties as a function of vertical electric field at $T = 300$ K. Hole carrier concentrations, p-type Seebeck coefficient, and electrical conductivity at the peak p-type ZT. The thermoelectric parameters are computed using an electron and hole mean free path, $\lambda = 88$ nm and a lattice thermal conductivity, κ_l, of 2000 W m^{-1} K^{-1}

Field (V/nm)	p ($\times 10^{12}$ cm^{-2})	S_p (μV K^{-1})	σ_p ($\times 10^7 \Omega$ m)$^{-1}$	ZT$_p$
0.0	0.06	73.4	0.53	0.0108
0.2	0.07	148.6	0.69	0.0161
0.4	0.08	152.6	0.73	0.0221
0.6	0.12	159.4	0.83	0.0271
0.8	0.14	179.1	0.94	0.0275
1.0	0.16	192.1	1.1	0.0281

of bilayer graphene subject to vertical electric fields ranging from 0.0 V/nm to 1.0 V/nm are summarized in Table XI. The p- and n-type thermoelectric parameters are similar.

D. Bi monolayer

The large spin-orbit interaction in bismuth leads to a Rasha-split dispersion of the valence band in a single monolayer of bismuth. The lattice parameters for the Bi(111) monolayer used for the SOC *ab-initio* calculations are summarized in Table I. The bandgap of the bismuth monolayer is 503 meV with the conduction band at Γ_c. The inclusion of spin-orbit interaction splits the two degenerate bands at Γ_v by 79 meV and deforms the valence band maxima into a Rashba split band. The calculated band structure of the Bi(111) monolayer is shown in Figures 9(a) and 9(b). The Rashba parameter for the bismuth monolayer is extracted from the *ab-initio* calculated band structure. The curvature of the valence band maxima of the Rashba band gives an effective mass of $m^* = 0.135$. The effective mass of the conduction band at Γ_c is $m^* = 0.008$. The vertical splitting of the bands at small k gives an $\alpha_R = 2.14$ eV Å. Prior experimental and theoretical studies on the strength of the Rashba interaction in Bi(111) surfaces find α_R values ranging from 0.55 eV Å^{-1} to 3.05 eV Å^{-1}.[57] A slight asymmetry in the Rashba-split dispersion leads to the valence band maxima lying along $\Gamma_v - M_v$. The band extremum along $\Gamma_v - K_v$ is 0.5 meV below the valence band maxima. The radius of the valence band-edge k_0, which is the distance from Γ_v to the band extremum along $\Gamma_v - M_v$ is 1.40 nm^{-1} similar to 4L InSe. The valence band-edge density of modes shown in Fig. 9(c) is a step function with a peak height of 0.96 nm^{-1}. Figure 9(d) shows the resulting thermoelectric figure of merit ZT as a function of Fermi level position at room temperature. The thermoelectric parameters at $T = 300$ K are summarized in Table XII.

There is one prior study of the thermoelectric performance of monolayer Bi.[79] In this study, Cheng *et al*. calculate a p-type (n-type) ZT of 2.4 (2.1), a peak p-type (n-type) Seebeck coefficient of 800 μV/K (-780 μV/K) using a lattice thermal conductivity of 3.9 W m^{-1} K^{-1}, and a relaxation time of 0.148 ps. We convert the relaxation time of 0.148 ps into an electron mean free path of 59.2 nm and a hole mean free path of 14.8 nm using average electron and hole thermal velocities of 4×10^5 m/s and 1×10^5, respectively, determined from the Bi(111) monolayer bandstructure. With these values for λ and a lattice thermal conductivity of 3.9 W m^{-1} K^{-1}, our calculation gives a peak p-type (n-type) ZT and Seebeck values of 1.9 (1.8) and 786 μV/K (-710 μV/K), respectively, which agrees well with the results in Ref. 79.

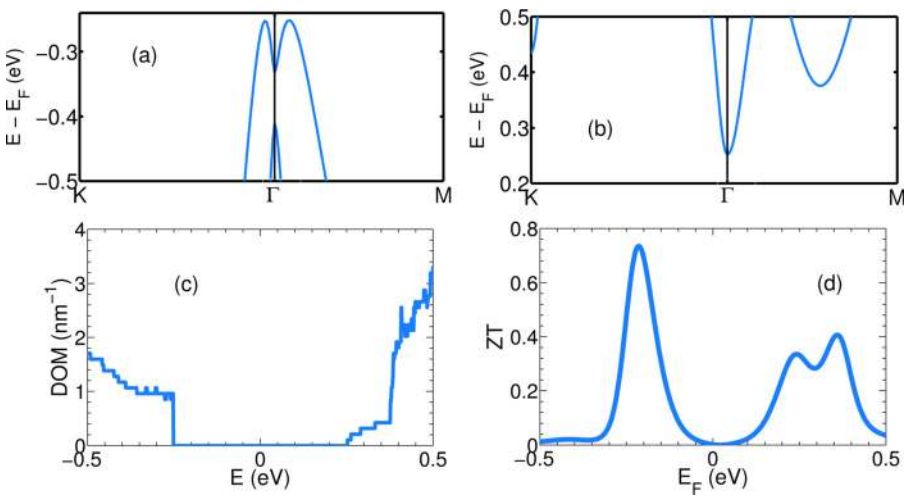

FIG. 9. Electronic structure and thermoelectric properties of Bi(111) monolayer. (a) Valence band, (b) conduction band of Bi(111) monolayer with spin-orbit interaction. (c) Density of modes with SOC interactions included. (d) Thermoelectric figure of merit, ZT, at room temperature.

TABLE XII. Bi(111) thermoelectric properties at $T = 300$ K. Hole and electron carrier concentrations (p and n), Seebeck coefficients (S$_p$ and S$_e$), and electrical conductivities (σ_p and σ_n) at the peak p- and n-type ZT. The thermoelectric parameters are computed using an electron and hole mean free path, $\lambda = 4.7$ nm and a lattice thermal conductivity, κ_l, of 3.9 W m^{-1} K^{-1}

p ($\times 10^{19}$ cm^{-3})	S_p (μV K^{-1})	σ_p ($\times 10^6 \Omega$ m)$^{-1}$	ZT$_p$	n ($\times 10^{19}$ cm^{-3})	$\lvert -S_e \rvert$ (μV K^{-1})	σ_e ($\times 10^6 \Omega$ m)$^{-1}$	ZT$_e$
0.61	239.7	0.19	0.73	0.35	234.1	0.089	0.41

IV. SUMMARY AND CONCLUSIONS

Monolayer and few-layer structures of III–VI materials (GaS, GaSe, InS, and InSe), Bi_2Se_3, monolayer Bi, and biased bilayer graphene all have a valence band that forms a ring in k-space. For monolayer Bi, the ring results from Rashba splitting of the spins. All of the other few-layer materials have valence bands in the shape of a "Mexican hat." For both cases, a band-edge that forms a ring in k-space is highly degenerate. It coincides with a singularity in the density of states and a near step-function turn-on of the density of modes at the band edge. The height of the step function is approximately proportional to the radius of the k-space ring.

As the radius of the k-space ring increases, the Fermi level at the maximum power factor or ZT moves higher into the bandgap away from the valence band edge. Nevertheless, the hole concentration increases. The average energy carried by a hole with respect to the Fermi energy increases. As a result, the Seebeck coefficient increases. The dispersion with the largest radius coincides with the maximum power factor provided that the mean free paths are not too different. For the materials and parameters considered here, the dispersion with the largest radius also results in the largest ZT at room temperature.

The Mexican hat dispersion in the valence band of the III–VI materials exists for few-layer geometries, and it is most prominent for monolayers, which have the largest radius k_0 and the largest height ϵ_0. The existence of the Mexican hat dispersions and their qualitative features do not depend on the choice of functional, stacking, or the inclusion or omission of spin-orbit coupling, and recent calculations by others show that they are also unaffected by many-electron self-energy effects.[13] At a thickness of 8 layers, all of the III–VI valence band dispersions are parabolic.

The Mexican hat dispersion in the valence band of monolayer Bi_2Se_3 is qualitatively different from those in the monolayer III–VIs. It can be better described as a double-brimmed hat characterized by 4 points of extrema that lie within $\sim k_BT$ of each other at room temperature. Furthermore, when two layers are brought together to form a bilayer, the energy splitting of the two valence bands in each layer causes the highest band to lose most of its outer ring causing a large decrease in the density of modes and reduction in the thermoelectric properties. These trends also apply to Bi_2Te_3.[50]

With the exception of monolayer GaS, the conduction bands of few-layer n-type III–VI and Bi_2Se_3 compounds are at Γ with a significant p_z orbital component. In bilayers and multilayers, these bands couple and split pushing the added bands to higher energy above the thermal transport window. Thus, the number of low-energy states per layer is maximum for a monolayer. In monolayer GaS, the conduction band is at M with 3-fold valley degeneracy. At thicknesses greater than a monolayer, the GaS conduction band is at Γ, the valley degeneracy is one, and the same splitting of the bands occurs as described above. Thus, the number of low-energy states per layer is also maximum for monolayer GaS. This results in maximum values for the n-type Seebeck coefficients, power factors, and ZTs at monolayer thicknesses for all of these materials.

ACKNOWLEDGMENTS

The *ab initio* calculations were supported by the National Science Foundation (NSF) Grant No. 1124733 and the Semiconductor Research Corporation (SRC) Nanoelectronic Research Initiative as a part of the Nanoelectronics for 2020 and Beyond (NEB-2020) program, and they used the Extreme Science and Engineering Discovery Environment (XSEDE), which is supported by National Science Foundation Grant No. ACI-1053575. The analytical theory development and analysis were supported by FAME, one of six centers of STARnet, a Semiconductor Research Corporation program sponsored by MARCO and DARPA.

[1]K. F. Mak, C. Lee, J. Hone, J. Shan, and T. F. Heinz, "Atomically thin MoS_2: A new direct-gap semiconductor," Phys. Rev. Lett. **105**, 136805 (2010).
[2]T. Stauber, N. M. R. Peres, F. Guinea, and A. H. Castro Neto, "Fermi liquid theory of a Fermi ring," Phys. Rev. B **75**, 115425 (2007).
[3]V. Zólyomi, N. D. Drummond, and V. I. Fal'ko, "Band structure and optical transitions in atomic layers of hexagonal gallium chalcogenides," Phys. Rev. B **87**, 195403 (2013).
[4]V. Zólyomi, N. D. Drummond, and V. I. Fal'ko, "Electrons and phonons in single layers of hexagonal indium chalcogenides from *ab initio* calculations," Phys. Rev. B **89**, 205416 (2014).
[5]F. Zhang, B. Sahu, H. Min, and A. H. MacDonald, "Band structure of a b c-stacked graphene trilayers," Phys. Rev. B **82**, 035409 (2010).
[6]A. Varlet, D. Bischoff, P. Simonet, K. Watanabe, T. Taniguchi, T. Ihn, K. Ensslin, M. Mucha-Kruczyński, and V. I. Fal'ko, "Anomalous sequence of quantum hall liquids revealing a tunable Lifshitz transition in bilayer graphene," Phys. Rev. Lett. **113**, 116602 (2014).
[7]Y. M. Blanter, M. I. Kaganov, A. V. Pantsulaya, and A. A. Varlamov, "The theory of electronic topological transitions," Phys. Rep. **245**, 159–257 (1994).
[8]X. G. Wang, L. Wang, J. Liu, and L. M. Peng, "Camel-back band-induced power factor enhancement of thermoelectric lead-tellurium from Boltzmann transport calculations," Appl. Phys. Lett. **104**, 132106 (2014).
[9]H. Peng, N. Kioussis, and G. Jeffrey Snyder, "Elemental tellurium as a chiral p-type thermoelectric material," Phys. Rev. B **89**, 195206 (2014).
[10]A. Takayama, T. Sato, S. Souma, and T. Takahashi, "Giant out-of-plane spin component and the asymmetry of spin polarization in surface rashba states of bismuth thin film," Phys. Rev. Lett. **106**, 166401 (2011).
[11]P. Hu, L. Wang, M. Yoon, J. Zhang, W. Feng, X. Wang, Z. Wen, J. C. Idrobo, Y. Miyamoto, D. B. Geohegan, and K. Xiao, "Highly responsive ultrathin GaS nanosheet photodetectors on rigid and flexible substrates," Nano Lett. **13**, 1649–1654 (2013).
[12]H. L. Zhuang and R. G. Hennig, "Single-layer group-III monochalcogenide photocatalysts for water splitting," Chem. Mater. **25**, 3232–3238 (2013).
[13]T. Cao, Z. Li, and S. G. Louie, "Tunable magnetism and half-metallicity in hole-doped monolayer gase," Phys. Rev. Lett. **114**, 236602 (2015).
[14]S. Wu, X. Dai, H. Yu, H. Fan, J. Hu, and W. Yao, "Magnetisms in *p*-type monolayer gallium chalcogenides (GaSe, GaS)," preprint arXiv:1409.4733 (2014).
[15]S. Lei, L. Ge, Z. Liu, S. Najmaei, G. Shi, G. You, J. Lou, R. Vajtai, and P. M. Ajayan, "Synthesis and photoresponse of large GaSe atomic layers," Nano Lett. **13**, 2777–2781 (2013).
[16]S. Lei, L. Ge, S. Najmaei, A. George, R. Kappera, J. Lou, M. Chhowalla, H. Yamaguchi, G. Gupta, R. Vajtai, A. Mohite, and P. Ajayan, "Evolution of the electronic band structure and efficient photo-detection in atomic layers of InSe," ACS Nano **8**(2), 1263–1272 (2014).
[17]P. Hu, Z. Wen, L. Wang, P. Tan, and K. Xiao, "Synthesis of few-layer GaSe nanosheets for high performance photodetectors," ACS Nano **6**, 5988–5994 (2012).
[18]D. J. Late, B. Liu, J. Luo, A. Yan, H. S. S. Matte, M. Grayson, C. N. R. Rao, and V. P. Dravid, "GaS and GaSe ultrathin layer transistors," Adv. Mater. **24**, 3549–3554 (2012).
[19]X. Li, M.-W. Lin, A. A. Puretzky, J. C. Idrobo, C. Ma, M. Chi, M. Yoon, C. M. Rouleau, I. I. Kravchenko, D. B. Geohegan, and K. Xiao,

"Controlled vapor phase growth of single crystalline, two-dimensional GaSe crystals with high photoresponse," Sci. Rep. **4**, 5497 (2014).
[20]M. Mahjouri-Samani, M. Tian, K. Wang, A. Boulesbaa, C. M. Rouleau, A. A. Puretzky, M. A. McGuire, B. R. Srijanto, K. Xiao, G. Eres, G. Duscher, and D. B. Geohegan, "Digital transfer growth of patterned 2D metal chalcogenides by confined nanoparticle evaporation," ACS Nano **8**, 11567–11575 (2014).
[21]F. Zahid and R. Lake, "Thermoelectric properties of Bi2Te3 atomic quintuple thin films," Appl. Phys. Lett. **97**, 212102 (2010).
[22]Y. Saeed, N. Singh, and U. Schwingenschlögl, "Thickness and strain effects on the thermoelectric transport in nanostructured Bi_2Se_3," Appl. Phys. Lett. **104**, 033105 (2014).
[23]H. Min, B. Sahu, S. K. Banerjee, and A. H. MacDonald, "*Ab initio* theory of gate induced gaps in graphene bilayers," Phys. Rev. B **75**, 155115 (2007).
[24]G. D. Mahan and J. O. Sofo, "The best thermoelectric," Proc. Natl. Acad. Sci. U.S.A. **93**, 7436–7439 (1996).
[25]J. P. Heremans, V. Jovovic, E. S. Toberer, A. Saramat, K. Kurosaki, A. Charoenphakdee, S. Yamanaka, and G. Jeffrey Snyder, "Enhancement of thermoelectric efficiency in pbte by distortion of the electronic density of states," Science **321**, 554–557 (2008).
[26]J. P. Heremans, B. Wiendlocha, and A. M. Chamoire, "Resonant levels in bulk thermoelectric semiconductors," Energy Environ. Sci. **5**, 5510–5530 (2012).
[27]A. Balandin and K. L. Wang, "Effect of phonon confinement on the thermoelectric figure of merit of quantum wells," J. Appl. Phys. **84**, 6149–6153 (1998).
[28]W. Kim, J. Zide, A. Gossard, D. Klenov, S. Stemmer, A. Shakouri, and A. Majumdar, "Thermal conductivity reduction and thermoelectric figure of merit increase by embedding nanoparticles in crystalline semiconductors," Phys. Rev. Lett. **96**, 045901 (2006).
[29]A. I. Hochbaum, R. Chen, R. D. Delgado, W. Liang, E. C. Garnett, M. Najarian, A. Majumdar, and P. Yang, "Enhanced thermoelectric performance of rough silicon nanowires," Nature **451**, 163–167 (2008).
[30]J.-H. Lee, J. Wu, and J. C. Grossman, "Enhancing the thermoelectric power factor with highly mismatched isoelectronic doping," Phys. Rev. Lett. **104**, 016602 (2010).
[31]M. Zebarjadi, K. Esfarjani, Z. Bian, and A. Shakouri, "Low-temperature thermoelectric power factor enhancement by controlling nanoparticle size distribution," Nano Lett. **11**, 225–230 (2011).
[32]L. D. Hicks and M. S. Dresselhaus, "Thermoelectric figure of merit of a one-dimensional conductor," Phys. Rev. B **47**, 16631–16634 (1993).
[33]M. S. Dresselhaus, G. Chen, M. Y. Tang, R. G. Yang, H. Lee, D. Z. Wang, Z. F. Ren, J.-P. Fleurial, and P. Gogna, "New directions for low-dimensional thermoelectric materials," Adv. Mater. **19**, 1043–1053 (2007).
[34]Y. Pei, X. Shi, A. LaLonde, H. Wang, L. Chen, and G. Jeffrey Snyder, "Convergence of electronic bands for high performance bulk thermoelectrics," Nature **473**, 66–69 (2011).
[35]J. R. Sootsman, D. Y. Chung, and M. G. Kanatzidis, "New and old concepts in thermoelectric materials," Angew. Chem. Int. Ed. **48**, 8616–8639 (2009).
[36]D. Wickramaratne, F. Zahid, and R. K. Lake, "Electronic and thermoelectric properties of few-layer transition metal dichalcogenides," J. Chem. Phys. **140**, 124710 (2014).
[37]M. K. Fuccillo, Q. D. Gibson, Mazhar N. Ali, L. M. Schoop, and R. J. Cava, "Correlated evolution of colossal thermoelectric effect and Kondo insulating behavior," APL Mater. **1**, 062102 (2013).
[38]P. Sun, N. Oeschler, S. Johnsen, B. B. Iversen, and F. Steglich, "Huge thermoelectric power factor: $FeSb_2$ versus $FeAs_2$ and $RuSb_2$," Appl. Phys. Express **2**, 091102 (2009).
[39]Y. Zhang, M. S. Dresselhaus, Y. Shi, Z. Ren, and G. Chen, "High thermoelectric figure-of-merit in Kondo insulator nanowires at low temperatures," Nano Lett. **11**, 1166–1170 (2011).
[40]Y. M. Blanter, A. A. Varlamov, A. V. Pantsulaya, and D. Parsons, "Thermoelectric power and topological transitions in quasi-2d electron systems," Sov. Phys., JETP **73**, 688–692 (1991).
[41]S. K. Firoz Islam and T. K. Ghosh, "Thermoelectric probe for the rashba spin–orbit interaction strength in a two dimensional electron gas," J. Phys.: Condens. Matter **24**, 345301 (2012).
[42]M. I. Alomar and D. Sánchez, "Thermoelectric effects in graphene with local spin-orbit interaction," Phys. Rev. B **89**, 115422 (2014).
[43]K. Mori, H. Sakakibara, H. Usui, and K. Kuroki, "Ideal band shape in the potential thermoelectric material $CuAlO_2$: Comparison to Na_xCoO_2," Phys. Rev. B **88**, 075141 (2013).
[44]K. Kuroki and R. Arita, "'pudding mold' band drives large thermopower in Na_xCoO_2," J. Phys. Soc. Jpn. **76**, 083707 (2007).
[45]M. M. Korshunov, I. Eremin, A. Shorikov, V. I. Anisimov, M. Renner, and W. Brenig, "Itinerant in-plane magnetic fluctuations and many-body correlations in Na_xCoO_2," Phys. Rev. B **75**, 094511 (2007).
[46]H. Usui, K. Suzuki, K. Kuroki, S. Nakano, K. Kudo, and M. Nohara, "Large seebeck effect in electron-doped $FeAs_2$ driven by a quasi-one-dimensional pudding-mold-type band," Phys. Rev. B **88**, 075140 (2013).
[47]D. Parker, X. Chen, and D. J. Singh, "High three-dimensional thermoelectric performance from low-dimensional bands," Phys. Rev. Lett. **110**, 146601 (2013).
[48]H. Shi, D. Parker, M.-H. Du, and D. J. Singh, "Connecting thermoelectric performance and topological-insulator behavior: Bi_2Te_3 and Bi_2Te_2Se from first principles," Phys. Rev. Appl. **3**, 014004 (2015).
[49]D. Parker and D. J. Singh, "Potential thermoelectric performance from optimization of hole-doped Bi_2Se_3," Phys. Rev. X **1**, 021005 (2011).
[50]J. Maassen and M. Lundstrom, "A computational study of the thermoelectric performance of ultrathin Bi_2Te_3 films," Appl. Phys. Lett. **102**, 093103 (2013).
[51]G. Zhou and D. Wang, "Few-quintuple Bi_2Te_3 nanofilms as potential thermoelectric materials," Sci. Rep. **5**, 8099 (2015).
[52]C. Jeong, R. Kim, M. Luisier, S. Datta, and M. Lundstrom, "On landauer versus Boltzmann and full band versus effective mass evaluation of thermoelectric transport coefficients," J. Appl. Phys. **107**, 023707 (2010).
[53]A. Paul, S. Salamat, C. Jeong, G. Klimeck, and M. Lundstrom, "An efficient algorithm to calculate intrinsic thermoelectric parameters based on landauer approach," J. Comput. Electron. **11**, 56–66 (2012).
[54]S. Datta, *Quantum Transport Atom to Transistor* (Cambridge University Press, Cambridge, 2005).
[55]R. Kim, S. Datta, and M. S. Lundstrom, "Influence of dimensionality on thermoelectric device performance," J. Appl. Phys. **105**, 034506 (2009).
[56]Y. A. Bychkov and E. I. Rashba, "Oscillatory effects and the magnetic susceptibility of carriers in inversion layers," J. Phys. C: Solid State Phys. **17**, 6039 (1984).
[57]K. Ishizaka, M. S. Bahramy, H. Murakawa, M. Sakano, T. Shimojima, T. Sonobe, K. Koizumi, S. Shin, H. Miyahara, A. Kimura, K. Miyamoto, T. Okuda, H. Namatame, M. Taniguchi, R. Arita, N. Nagaosa, K. Kobayashi, Y. Murakami, R. Kumai, Y. Kaneko, Y. Onosoe, and Y. Tokura, "Giant rashba-type spin splitting in bulk BiTeI," Nat. Mater. **10**, 521–526 (2011).
[58]P. E. Blöchl, "Projector augmented-wave method," Phys. Rev. B **50**, 17953–17979 (1994).
[59]J. P. Perdew, K. Burke, and M. Ernzerhof, "Generalized gradient approximation made simple," Phys. Rev. Lett. **77**, 3865–3868 (1996).
[60]M. Ernzerhof and G. E. Scuseria, "Assessment of the Perdew-Burke-Ernzerhof exchange-correlation functional," J. Chem. Phys. **110**, 5029–5036 (1999).
[61]G. Kresse and J. Hafner, "*Ab initio* molecular dynamics for open-shell transition metals," Phys. Rev. B **48**, 13115–13118 (1993).
[62]G. Kresse and J. Furthmuller, "Efficiency of *ab-initio* total energy calculations for metals and semiconductors using a plane-wave basis set," Comput. Mater. Sci. **6**, 15–50 (1996).
[63]S. Grimme, "Semiempirical GGA-type density functional constructed with a long-range dispersion correction," J. Comput. Chem. **27**, 1787–1799 (2006).
[64]J. Heyd, G. E. Scuseria, and M. Ernzerhof, "Hybrid functionals based on a screened coulomb potential," J. Chem. Phys. **118**, 8207–8215 (2003).
[65]A. Kuhn, A. Chevy, and R. Chevalier, "Refinement of the 2h gas-type," Acta Crystallogr., Sect. B **32**, 983–984 (1976).
[66]A. Kuhn, A. Chevy, and R. Chevalier, "Crystal structure and interatomic distances in gase," Phys. Status Solidi A **31**, 469–475 (1975).
[67]C. De Blasi, G. Micocci, S. Mongelli, and A. Tepore, "Large inse single crystals grown from stoichiometric and non-stoichiometric melts," J. Cryst. Growth **57**, 482–486 (1982).
[68]S. Nakajima, "The crystal structure of Bi_2Te_3-xSe_x," J. Phys. Chem. Solids **24**, 479–485 (1963).
[69]T. Ohta, A. Bostwick, T. Seyller, K. Horn, and E. Rotenberg, "Controlling the electronic structure of bilayer graphene," Science **313**, 951–954 (2006).
[70]F. I. Ismailov, G. A. Akhundov, and O. R. Vernich, "Investigation of electrical conductivity and Hall effect in GaSe single crystals," Phys. Status Solidi B **17**, K237–K240 (1966).
[71]G. Micocci, R. Rella, P. Siciliano, and A. Tepore, "Investigation of electronic properties of gallium sulfide single crystals grown by iodine chemical transport," J. Appl. Phys. **68**, 138–142 (1990).

[72]D. V. Krishna and P. Jayarama Reddy, "Electrical conductivity, structure and hall effect measurements of InSe films," Thin Solid Films **105**, 139–147 (1983).
[73]R. S. Mane and C. D. Lokhande, "Studies on structural, optical and electrical properties of indium sulfide thin films," Mater. Chem. Phys. **78**, 15–17 (2003).
[74]R. A. Hoffman and D. R. Frankl, "Electrical transport properties of thin bismuth films," Phys. Rev. B **3**, 1825 (1971).
[75]Y. S. Hor, A. Richardella, P. Roushan, Y. Xia, J. G. Checkelsky, A. Yazdani, M. Z. Hasan, N. P. Ong, and R. J. Cava, "*p*-type Bi_2Se_3 for topological insulator and low-temperature thermoelectric applications," Phys. Rev. B **79**, 195208 (2009).
[76]C.-R. Wang, W.-S. Lu, L. Hao, W.-L. Lee, T.-K. Lee, F. Lin, I-C. Cheng, and J.-Z. Chen, "Enhanced thermoelectric power in dual-gated bilayer graphene," Phys. Rev. Lett. **107**, 186602 (2011).
[77]M. A. Alzhdanov, M. D. Nadzhafzade, and Z. Yu Seidov, "Thermal conductivity of gallium sulfide," Phys. Solid State **41**, 20–21 (1999).
[78]D. P. Spitzer, "Lattice thermal conductivity of semiconductors: A chemical bond approach," J. Phys. Chem. Solids **31**, 19–40 (1970).
[79]L. Cheng, H. Liu, X. Tan, J. Zhang, J. Wei, H. Lv, J. Shi, and X. Tang, "Thermoelectric properties of a monolayer bismuth," J. Phys. Chem. C **118**, 904 (2014).
[80]H. Julian Goldsmid, *Introduction to Thermoelectricity* (Springer, 2009), Vol. 121.
[81]A. A. Balandin, "Thermal properties of graphene and nanostructured carbon materials," Nat. Mater. **10**, 569–581 (2011).
[82]B. D. Kong, S. Paul, M. Buongiorno Nardelli, and K. W. Kim, "First-principles analysis of lattice thermal conductivity in monolayer and bilayer graphene," Phys. Rev. B **80**, 033406 (2009).
[83]R. Yan, J. R. Simpson, S. Bertolazzi, J. Brivio, M. Watson, X. Wu, A. Kis, T. Luo, A. R. Hight Walker, and H. Grace Xing, "Thermal conductivity of monolayer molybdenum disulfide obtained from temperature-dependent Raman spectroscopy," ACS Nano **8**, 986–993 (2014).
[84]B. Qiu and X. Ruan, "Thermal conductivity prediction and analysis of few-quintuple Bi_2Te_3 thin films: A molecular dynamics study," Appl. Phys. Lett. **97**, 183107 (2010).
[85]W. Li, J. Carrete, and N. Mingo, "Thermal conductivity and phonon linewidths of monolayer MoS_2 from first principles," Appl. Phys. Lett. **103**, 253103 (2013).
[86]S. Ghosh, W. Bao, D. L. Nika, S. Subrina, E. P. Pokatilov, C. N. Lau, and A. A. Balandin, "Dimensional crossover of thermal transport in few-layer graphene," Nat. Mater. **9**, 555–558 (2010).
[87]J. He, K. Hummer, and C. Franchini, "Stacking effects on the electronic and optical properties of bilayer transition metal dichalcogenides MoS_2, $MoSe_2$, WS_2, and WSe_2," Phys. Rev. B **89**, 075409 (2014).
[88]Z. Zhu, Y. Cheng, and U. Schwingenschlögl, "Topological phase transition in layered GaS and GaSe," Phys. Rev. Lett. **108**, 266805 (2012).
[89]W. An, F. Wu, H. Jiang, G.-S. Tian, and X.-Z. Li, "Systematic investigation on topological properties of layered *gas* and *gase* under strain," J. Chem. Phys. **141**, 084701 (2014).
[90]Y. L. Chen, J. G. Analytis, J.-H. Chu, Z. K. Liu, S.-K. Mo, X. L. Qi, H. J. Zhang, D. H. Lu, X. Dai, Z. Fang, S. C. Zhang, I. R. Fisher, Z. Hussain, and Z.-X. Shen, "Experimental realization of a three-dimensional topological insulator, Bi_2Te_3," Science **325**, 178–181 (2009).
[91]G. Yin, D. Wickramaratne, and R. K. Lake, "Tunneling spectroscopy of chiral states in ultra-thin topological insulators," J. Appl. Phys. **113**, 063707 (2013).
[92]D. Hseih, D. Qian, L. Wray, Y. Xia, Y. S. Hor, R. J. Cava, and M. Z. Hasan, "A topological Dirac insulator in a quantum spin hall phase," Nature **452**, 970–974 (2008).
[93]V. Goyal, D. Teweldebrhan, and A. A. Balandin, "Mechanically-exfoliated stacks of thin films of Bi_2Te_3 topological insulators with enhanced thermoelectric performance," Appl. Phys. Lett. **97**, 133117 (2010).
[94]J. G. Checkelsky, Y. S. Hor, R. J. Cava, and N. P. Ong, "Bulk band gap and surface state conduction observed in voltage-tuned crystals of the topological insulator Bi_2Se_3," Phys. Rev. Lett. **106**, 196801 (2011).
[95]Y. Zhang, K. He, C.-Z. Chang, C.-L. Song, L.-L. Wang, X. Chen, J.-F. Jia, Z. Fang, X. Dai, W.-Y. Shan, S.-Q. Shen, Q. Niu, X.-L. Qi, S.-C. Zhang, X.-C. Ma, and Q.-K. Xue, "Crossover of the three-dimensional topological insulator Bi_2Se_3 to the two-dimensional limit," Nat. Phys. **6**, 584–588 (2010).
[96]W. Liu, X. Peng, X. Wei, H. Yang, G. Malcolm Stocks, and J. Zhong, "Surface and substrate induced effects on thin films of the topological insulators Bi_2Se_3 and Bi_2Te_3," Phys. Rev. B **87**, 205315 (2013).
[97]Y. Zhang, T.-T. Tang, C. Girit, Z. Hao, M. C. Martin, A. Zettl, M. F. Crommie, Y. Ron Shen, and F. Wang, "Direct observation of a widely tunable bandgap in bilayer graphene," Nature **459**, 820 (2009).
[98]E. McCann, "Asymmetry gap in the electronic band structure of bilayer graphene," Phys. Rev. B **74**, 161403R (2006).